Analysis of Hydrogen Peroxide Production in Nanosecond Pulsed Discharges in Water

Bachelor Thesis

in the
degree program
"Bachelor of Science"
in Physics

at the Faculty of Physics and Astronomy
of the Ruhr-Universität Bochum

by
Chaiyasit Nenbangkaeo

from
Nong Bua Lam Phu
Thailand

Bochum 2019

Zusammenfassung

Gepulste Entladungen in Flüssigkeiten bieten breite Anwendungsfelder in der Medizin, Biologie, Chemie, Elektrochemie und Umwelt. Dies erklärt ihre intensive Untersuchung in der Forschung. Hochspannungspulse mit Anstiegszeiten von einigen Nanosekunden und einem starken elektrischen Feld an der Elektrode sind in der Lage, Wasser effizient zu dissoziieren und zu ionisieren. Chemische Spezies werden gebildet und können z.B. mit Verunreinigungen oder Oberflächen in der Flüssigkeit reagieren. Der Erwärmungsprozess des Wassers während des Pulses entfällt, wenn der Puls und die Anstiegszeit kurz genug sind und bei der Zündung der Entladung erreicht das Wassser überkritischen Zustand.

In dieser Arbeit werden Einflüsse der Behandlungszeit, Entladungsfrequenz und Entladungsspannung auf die Wasserstoffperoxidproduktion in destilliertem Wasser untersucht. Absorptionsspektroskopie in Kombination mit einer kalorimetrischen Methode wird verwendet, um Wasserstoffperoxid zu messen. Die Abhängigkeit der Wasserstoffperoxidproduktion von dem Parameter Entladungsspannung ist sigmoidal, aber linear für Behandlungszeit und Entladungsfrequenz. Bei einer Entladungsspannung von 20 kV, einer Entladungsfrequenz von 15 Hz und einer Behandlungszeit von 10 min ist die Wasserstoffperoxidkonzentration $(30 \pm 7)\,\mu\mathrm{mol\,L^{-1}}$. Die Spannung, die zu einer maximalen Wasserstoffperoxidproduktionrate führt, liegt bei 21 kV. Mit der Einführung eines globalen kinetischen Models wird die zeitlich abhängige Konzentration verschiedener Spezies wie z. B. H, OH und H_2O_2 berechnet.

Unter Betrachtung des angenommenen vollständig ioinisierten Wasser mit einer Initialdichte von $3 \times 10^{28}\,\mathrm{m^{-3}}$, ist das Plasma im Quantenzustand. Mit Hilfe der Fermi-Dirac Statistik und der Kavitationstheorie kann eine Initialtemperatur von ca. 8000 K für 21 kV abgeschätzt werden.

Abstract

Pulsed discharges in liquids provide wide application fields in medicine, biology, chemistry, electrochemistry and environment. This explains their intensive investigation in research. High voltage pulses with rise times of a few nanoseconds and high electric fields at the electrode are able to dissociate and to ionize water efficiently. Chemical species are formed and can e.g. react with contaminants or surfaces present in the liquid. The heating process of the water during the pulse is eliminated if the pulse and rise time are short enough and the water reaches supercritical state at the ignition.

In this thesis, the influences of treatment time, discharge frequency and discharge voltage on hydrogen peroxide production in distilled water are investigated. Absorption spectroscopy in combination with a colorimetric method is used to measure hydrogen peroxide. The dependence of hydrogen peroxide production on the parameter discharge voltage is sigmoidal, but linear for treatment time and discharge frequency. At a discharge voltage of 20 kV, a discharge frequency of 15 Hz and a treatment time of 10 min, the hydrogen peroxide concentration is $(30 \pm 7)\,\mu\mathrm{mol\,L^{-1}}$. The voltage which lead to maximal hydrogen peroxide production rate is 21 kV. With the introduction of a global kinetic model, the time-dependent concentration of different species such as H, OH and H_2O_2 is calculated.

Considering the assumed fully ionized water with an initial density of $3 \times 10^{28}\,\mathrm{m^{-3}}$, the plasma is in quantum state. Using the Fermi-Dirac statistic and the cavitation theory, an initial temperature of approx. 8000 K for 21 kV can be estimated.

Contents

List of Figures

1 Motivation

Pulsed discharges in liquids have been subject of attention in the field of plasma science, biology, chemistry and technology. They offer wide range of applications such as the destruction of microorganisms [1], water treatment [2, 3] and shockwave formation [4].

Over the last decade, the interest of plasma-liquid interactions are broadened to growth of nanoparticles [5, 6], chemical synthesis [7] and environmental sector [8]. Because of water pollution due to the use of pesticides in agriculture [9] and hardly degradable textile dye by the industry [10], water purification has become the main focus of investigation. Conventional water purification with ozone treatment, filtration and chemicals are not able to decontaminate all microorganism and toxins. Radical species like hydroxyl and hydrogen peroxide produced by pulsed discharges at high voltages in water can overcome weaknesses of the current water purification [1, 8]. Especially, hydroxyl is highly efficient in case of organic compound mineralization [8]. Besides radicals, UV radiation and shockwaves are generated during pulsed discharges [11]. Nanosecond pulses with short rise times lead to instant plasma state formation and might be more efficient for species creation than microsecond pulsed or plasma-gas-liquid systems [12].

Plasma-liquid interactions are of complex nature and cannot be investigated easily without influencing the system. Despite intensive research on different discharge setups [7, 12–16], there is still no agreement on comprehensive theory for the description of the physics and chemistry.

Examination of nanosecond pulsed discharges are challenging due to short duration and small geometrical dimension of the created bubble. Nonetheless, optical emission spectroscopy, shadowgraphy and schlieren imaging can give information about the chemical composition, breakdown and for monitoring shockwave formation inside the liquid which is used for pressure estimations. Measurement of electrical properties of nanosecond pulse discharges can be performed with a back current shunt [17]. Information about oxidation effects of a system can be received by hydrogen peroxide measurement.

For the first time, investigation of the hydrogen peroxide production and its evolution for a 10 ns pulsed discharges in a pin-to-pin setup in distilled water is realized in this thesis.

For the measurement of hydrogen peroxide, absorption spectroscopy is performed in combination with colorimetry. Treatment time, discharge frequency, discharge voltage and electrode gap distance which influence the hydrogen peroxide formation are studied for better prediction of the hydrogen peroxide density. Moreover, a modeling of the species created during the discharge process is performed and compared to the measured hydrogen peroxide density. Consideration of different energy distributions of the electrons at ignition is realized. The initial temperature is calculated according to this consideration.

Results from the measurements and the modeling participate to better understanding of the species creation during nanosecond pulsed discharges. Further investigations can improve the model to achieve better prediction of the created species. The extreme properties of these discharges lead to changes in the fundamental considerations of the plasma properties at ignition.

2 State of the Art

In this chapter, the state of the art for the performed study is presented. First, the definition of a plasma is given. Then, the breakdown mechanism is described. The discharge configuration and breakdown mechanism in liquid and parameters are taken into account in the explanation of the discharge in liquid. Next, the cavitation theory as well as the evolution of the discharge in the nanosecond pulse are explained. The chemical reactions in the discharge channel are described at the end.

2.1 Definition of a plasma

A plasma is a state of partly ionized gas with neutral and charged particles. From a macroscopic view, it is quasi-neutral and shows collective behavior. Within a specific scale individual charges can be perceived. The following conditions define a plasma state:

The Debye length λ_D is the length of the shielding of the plasma:

$$\lambda_\mathrm{D} = \sqrt{\frac{\epsilon_0 k_\mathrm{B} T_\mathrm{e}}{n e^2}}. \tag{2.1}$$

The vacuum permittivity is given by ϵ_0, the Boltzmann constant is k_B, the temperature of the electrons in the plasma is T_e, the density is n and the elementary charge is e. To guarantee quasi-neutrality, the dimension of the plasma L must be greater than the Debye length:

$$L \gg \lambda_\mathrm{D}. \tag{2.2}$$

Local changes in the density of charged particles are shielded on a scale smaller than L if the condition above is fulfilled.

A volume with the radius of the Debye length can be defined as the Debye sphere V_D.

$$V_\mathrm{D} = \frac{4}{3}\pi\lambda_\mathrm{D}^3 \tag{2.3}$$

To ensure collective behavior, the number of particles inside this Debye sphere N_D must be much larger than one. This condition is expressed by

$$N_\mathrm{D} = \frac{4}{3}\pi\lambda_\mathrm{D}^3 n \gg 1. \tag{2.4}$$

Charged particles react to changes in the plasma with plasma oscillation at the plasma frequency w_P.

$$w_\mathrm{P} = \sqrt{\frac{n_\mathrm{e} e^2}{\epsilon_0 m}} \tag{2.5}$$

The effective mass of the electrons or ions is m. In a plasma, the electromagnetic force is the dominating force where else hydrodynamic forces are prevalent in gases. The product of the plasma frequency w_P and the mean free time of two neutral particles τ must be greater than one:

$$w_\mathrm{P}\tau \gg 1. \tag{2.6}$$

2.2 Breakdown mechanism

Within a gas filled gap, free electrons accelerate to the anode if an electric field is applied. These electrons are able to ionize the species in the surrounding gas inducing an electron avalanche allowing the ignition of a plasma. For low pressure and short gaps ($p \cdot d < 4000\,\mathrm{Torr\,cm}$) Townsend breakdown occurs [18, 19]. Ionization of the surrounding gas is caused by electron avalanches. This process starts with the acceleration of free electrons towards the electric field direction. If their energy is high enough, they can ionize atoms and molecules by collision. This releases additional electrons which experience the same acceleration and therefore collide with further atoms. A chain reaction has started and an electron avalanche occurs. For the plasma to ignite, the same amount of electrons at the origin of the avalanches needs to be replaced by new electrons. These new electrons are the result of secondary electron emission caused by impinging ions at the cathode. As long as this criteria is fulfilled and the voltage is applied, the plasma is self-sustained.

In larger gaps and for higher pressures, spark or streamer breakdown mechanisms take place. Sparks are breakdowns in a narrow channel and are related to avalanches. Streamers are thin ionized channels with conducting and filamentary luminous structures which propagate quickly between electrodes in a positive charged path of previous primary avalanches. The mechanism of the avalanche is the same as for the Townsend breakdown but with a higher electron density. The density of charged particles induces an electric field of the same order of magnitude as the electrical field given by the geometrical configuration of the electrodes. This influences the evolution of the avalanches in comparison to the Townsend breakdown. Photons generated by the primary avalanches initiate secondary avalanches. The electrons of the latter get pulled by the positive charged trail of the primary avalanches initiating a positive streamer [18–20].

2.3 Discharge in liquid

Discharges in liquids are challenging to investigate due to their complex interactions of plasma and liquid. No consistent description of the discharge behavior and plasma properties are existing yet. Influences of the experimental parameters on the discharge are not fully understood. This section gives an overview of the discharge configurations, behaviors and parameters.

2.3.1 Discharge configuration

Non-thermal plasma-liquid interaction can be realized by several setups. Commonly, these configurations consist of a metal pin or plate electrode placed in or outside of the liquid and are powered by AC, DC or HV pulses. In addition, the conditions for the plasma can be changed by bubbling a gas inside the liquid which induces breakdown within the gas bubbles. Therefore, the different types of reactors can be summarized to direct liquid phase discharges (a), discharges in gas phase with liquid electrode (b) and direct liquid phase discharges with additional bubbles (c) (see fig.2.1) [14].

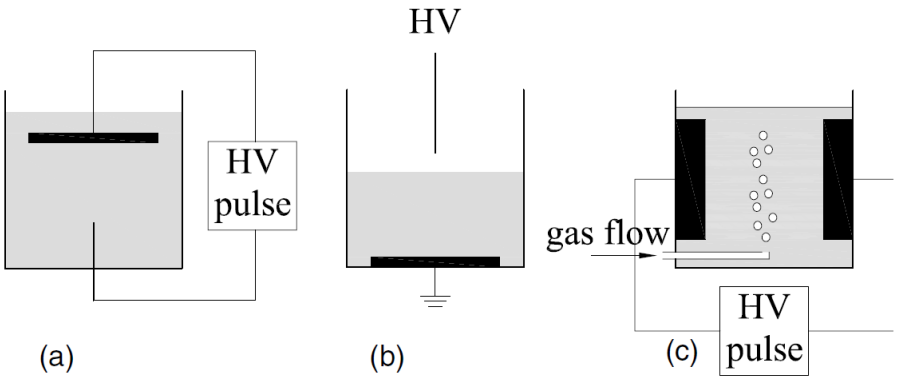

Figure 2.1: Three different electrode configurations for plasma-liquid interactions. (a) direct liquid phase discharge reactor (b) gas phase discharge reactor with liquid electrode (c) example of bubble discharge reactor [14].

In case of the direct liquid phase discharge reactor, both electrodes are placed in the liquid. Figure 2.1a shows a pin-to-plate configuration where else a pin-to-pin configuration is also common. If one electrode is positioned above the liquid surface and the liquid acts as an electrode (fig. 2.1b), the discharge ignites in gas phase and interacts with the liquid. In these gas phase discharge reactors, the electrode properties are different to the first type as the secondary electron emission of water is smaller compared to metals. Ignition can take place in liquid with bubbles, too (fig. 2.1c). These reactors are similar to the direct liquid phase reactor. More information about plasma-liquid interactions can be found in literature [13, 14].

2.3.2 Breakdown mechanism in liquid and parameters

Formation of plasmas in liquids depends on various parameters, which influence the breakdown. These parameters are electrode configuration, material and shape, liquid properties, applied voltage and the shape and width of the pulse [13, 21, 22]. In addition, the length and properties of the cable connecting the pulse generator and the electrode affect the discharge in nanosecond pulses [12]. As the breakdown occurs at the electrode tip, the electric field $\vec{E}$ is proportional to the stressed electrode area A as well as the stress time t.

$$E \propto A^{-n} t^{-\frac{1}{3}} \tag{2.7}$$

The constant n is depending on the liquid properties and electrode gap distance [22, 23].

For liquid as a plasma medium, the amount of free electrons is significantly less than in gas. Therefore, electron avalanches in bulk water are almost negligible as the high electric field region close to the electrode and the large scattering cross section result in kinetic energy not high enough for ionization [14]. Free electrons vanish within picosecond if they are present [24].

For in-liquid discharges created by microsecond pulses, a micro-bubble forms at the tip of the driven electrode within microseconds, which is the starting point for the electrical breakdown [25, 26]. From this gaseous phase, large electrical fields due to electrohydrodynamic instability of the bubble-water interface yield the break up of the bubble and streamers formation [27, 28].

In case of nanosecond pulses, however, the discharge cause a high field region at the driven electrode which assists thermal dissociation of water into conductive species. This conductive region is able to ionize surrounding regions and a breakdown mechanism is initiated with this ionization wave [29]. Preexisting nanopores help the streamer to propagate after previously mentioned effects occur [14].

According to Tereshonok et al. [30], pre-breakdown and breakdown phenomema can be summarized in four time scales. Within the order of 1 ns, in the first time scale, pre-breakdown processes like cavitation void, cavitation bubbles and townsend breakdown take place. In the second time scale, liquid vapor fills the cavitation bubble. In the conductive region, breakdown phenomena such as the streamer breakdown occur between 10 µs to 30 µs during the third time scale. The fourth time scale is characterized by the slow thermal breakdown of duration in ms.

Marinov et al. [31] observed bush-like and tree-like streamers. Micro cavities form at the rising and/or falling edge of the high voltage pulses around the breakdown voltage. Bush-like streamers ignite in this cavity tree-like and streamers seem to ignite directly inside the liquid.

2.4 Cavitation theory

In a recent study, Grosse et al. [12] have used cavitation theory, shadowgraphy and optical emission spectroscopy to investigate plasma generation in 10 ns pulses with both electrodes emerged in distilled water of $2\,\mu S\,cm^{-1}$ conductivity.

Cavitation occurs as a result of local pressure differences in liquids caused by fast moving objects or electrical breakdown at high voltage and bubbles are formed. Pressure differences and surface tension are the acting forces at the bubble surface, they are considered in the derivation of the expansion of the bubble. The starting point of the derivation is the Rayleigh-Plesset equation which describes the expansion of a spherical bubble inside compressible liquids with pressure pulse propagation at sound velocity [32–35]. This equation is simplified to:

$$R\ddot{R}\left(1-\frac{\dot{R}}{C}\right)+\frac{3}{2}\dot{R}^2\left(1-\frac{\dot{R}}{3C}\right)=h\left(1+\frac{\dot{R}}{C}\right) \tag{2.8}$$

The bubble radius is R, C is the speed of sound at the radius interface and h is the enthalpy. The calculation of C and h can be seen in [12].

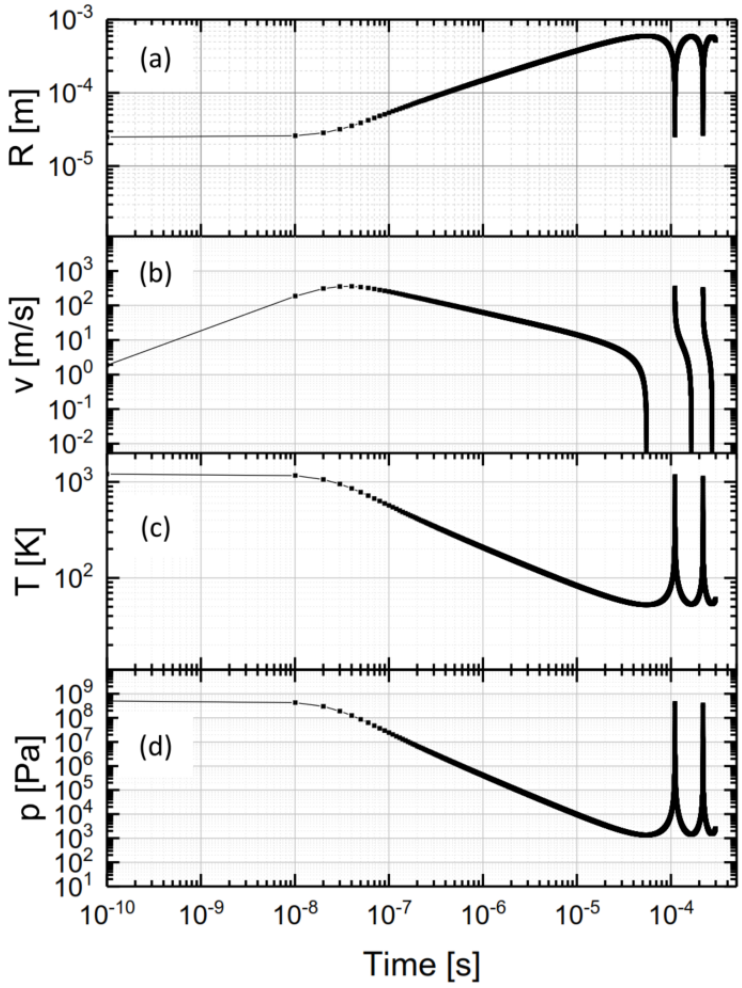

Figure 2.2: Numerical solution of equation 2.8 with initial radius $R_0 = 25\,\mu\text{m}$, initial pressure $p_0 = 5 \times 10^8\,\text{Pa}$ and initial velocity $\dot{R}_0 = 0$: (a) bubble radius $R(t)$, (b) bubble radius velocity $\dot{R}(t)$, (c) temperature of the gas inside the buble $T(t)$ with initial temperature $T_0 = 1200\,\text{K}$, (d) pressure $p(t)$ of the gas inside the bubble [12].

Based on this equation, the bubble radius $R(t)$, the bubble radius velocity $\dot{R}(t)$, the temperature of the adiabatic expansion $T(t)$ and the pressure inside the liquid $p_{\text{liquid}}(R)$ can be calculated.

$$p_{\text{liquid}}(R) = \frac{1}{2}\epsilon_0 E_{\text{HV}}^2 \left(1 - \frac{1}{\epsilon_{\text{water}}} + \frac{k}{\epsilon_{\text{water}}}\right) + p_{0,\text{gas}} \left(\frac{R_0}{R}\right)^{3\gamma} - \frac{2\sigma}{R} - 4\eta\frac{\dot{R}}{R} \tag{2.9}$$

The electrical field constant is ϵ_0, the dielectric constant of water is $\epsilon_{\text{water}} = 80$, $k = 1.5$ is the coefficient taking into account electrostriction [36], $p_{0,\text{gas}}$ is a free parameter, $\gamma = 1.33$ is the adiabatic coefficient of water, σ is the surface tension and η the viscosity of water and $E_{\text{HV}} = U_{\text{HV}}/R_0$ is the electric field at the tungsten tip surface. The initial temperature at an initial bubble radius R_0 is T_0.

$$T(t) = T_0 \left(\frac{R_0}{R(t)}\right)^{3(\gamma-1)} \tag{2.10}$$

The solved numerical solution of equation 2.8 with an initial pressure of $p_0 = 5 \times 10^8\,\text{Pa}$, and initial radius of $R_0 = 25\,\mu\text{m}$ an the initial velocity $\dot{R}_0 = 0$ can be

seen in figure 2.2. (a) is the bubble radius $R(t)$, (b) is the bubble radius velocity $\dot{R}(t)$, (c) is the temperature of the gas inside the bubble $T(t)$ with an initial temperature $T_0 = 1200\,\mathrm{K}$ and (d) is pressure $p(t)$ of the gas inside the bubble. Within the pulse duration of $t_{\mathrm{pulse}} = 10\,\mathrm{ns}$ the bubble size stays almost constant. At 50 ns, the maximal velocity of $400\,\mathrm{m\,s^{-1}}$ is reached. The maximum bubble size of 600 µm is reached at 50 µs. Due to the adiabatic expansion, the pressure dropped to $10^3\,\mathrm{Pa}$ and the temperature to $T = 0.05\,T_0$ at the latter mentioned time. At 100 µs, the bubble collapses.

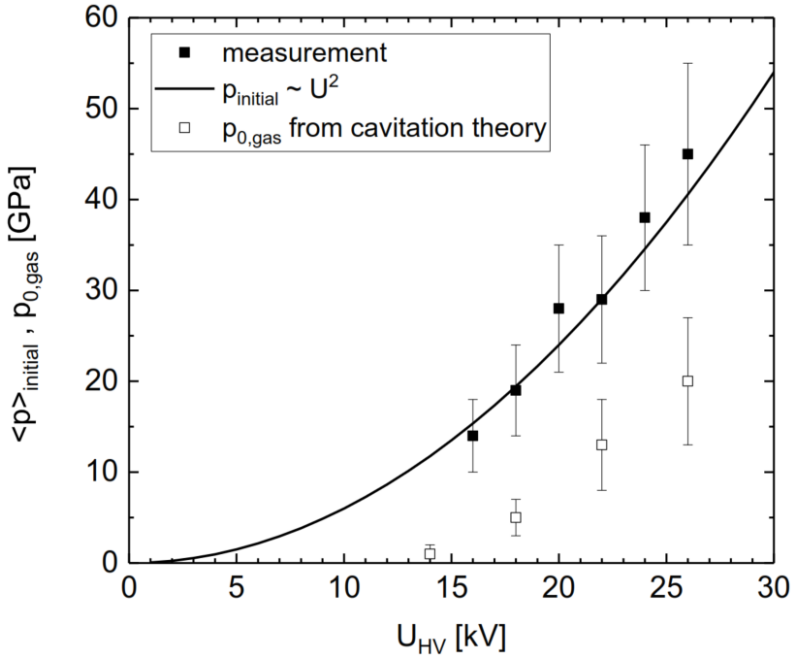

Figure 2.3: Analysis of the emitted propagation of the soundwave: average initial pressure $\langle p_{\mathrm{initial}} \rangle$ within the first 44 ns after ignition derived from propagation velocities of the initial sound wave as a function of the ignition voltage U_{HV}. A scaling of $\langle p_{\mathrm{initial}} \rangle \propto U\mathrm{HV}^2$ is the solid line. $p_{0,\mathrm{gas}}$ is the fitting pressure inside an initial bubble with radius 25 µm to model the expansion of the cavitation bubble (open symbols) [12].

Moreover, the fitting initial pressure $p_{0,\mathrm{gas}}$ in dependency to the discharge voltage U_{HV} inside the initial bubble of 25 µm is fitted to model the expansion of the cavitation bubble. It can be seen in figure 2.3. $p_{0,\mathrm{gas}}$ is a free parameter and has been set for the best fitting result according to bubble size measurements with shadowgraphy.

Evolution of the discharge in nanosecond pulse

The mechanism of the discharge can be seen in fig. 2.4 and can be summarized as follows: (a) At a radius of approximately 5 µm at the tip of the electrode after 1 ns, a local negative pressure causes the liquid to rapture to nanopores and the ignition takes place in latter with a water molecule density of $3.3 \times 10^{28}\,\mathrm{m^{-3}}$. Due to electrical energy dissipation, the liquid within mentioned radius converts instantly into plasma state. With a dissipated energy of $3.2 \times 10^{-5}\,\mathrm{J}$ [12], complete ionization of the water can be assumed and high pressure initiates cavitation and the bubble

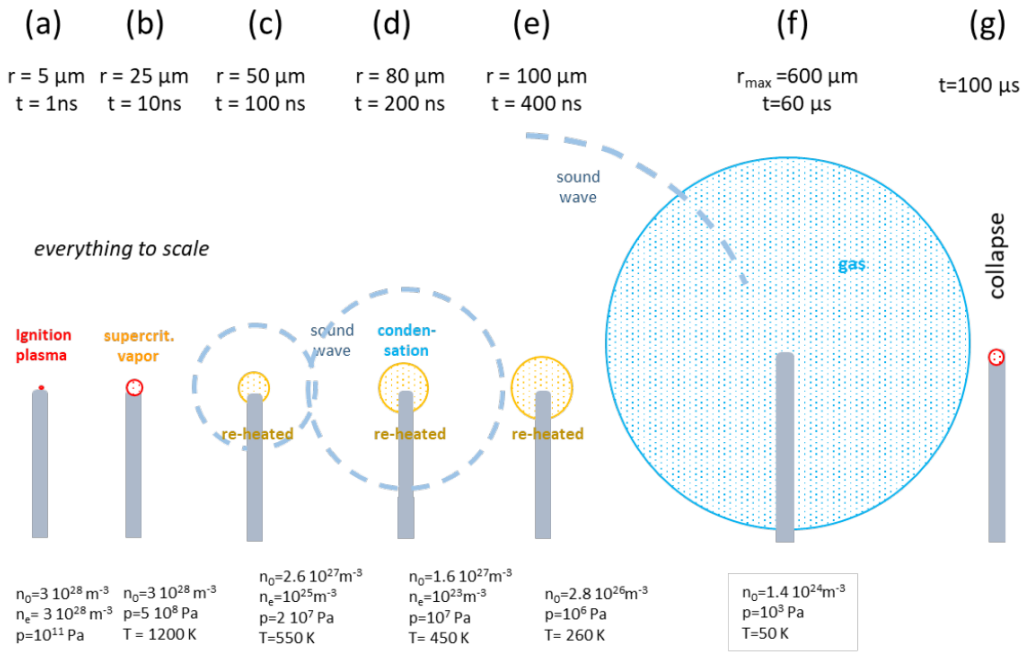

Figure 2.4: Schematic of bubble properties during expansion: (a) ignition creating the initial bubble with 5 µm radius, (b) pressure and temperature release creates initial super critical water bubble with $R_0 = 25\,\mu\text{m}$ radius at $p_0 = 5 \times 10^8\,\text{Pa}$ and $T = 1200\,\text{K}$, (c) adiabatic expansion of the bubble at 50 µm radius at $p = 2 \times 10^7\,\text{Pa}$ and $T = 550\,\text{K}$, (d) at 80 µm at $p = 10^7\,\text{Pa}$ and $T = 450\,\text{K}$ condensation set in and bubble reaches critical point. (e) at 100 µm at $p = 10^6\,\text{Pa}$ and $T = 260\,\text{K}$, (f) at maximum radius of 600 µm at $p = 10^3\,\text{Pa}$ and $T = 50\,\text{K}$, (g) collapse at $t = 100\,\mu\text{s}$ [12]

expanses. (b) Within a bubble of 25 µm radius size and a temperature of 1200 K, the vapor is now in a super critical state at liquid water molecules density after 10 ns. The pressure is of $0.5 \times 10^9\,\text{Pa}$. (c) After the pulse, this bubble expands adiabatically. The sound waves caused by the initial pressure propagate through the water from this point. High voltage power oscillation between the power supply and the chamber re-ignites the plasma. (d)-(f) Due to condensation, the bubble reaches its critical point and the pressure and temperature drop. The maximum size of 1.2 mm is reached after 100 µs. The temperature and pressure drop to 50 K and 10 mbar after 60 µs. (g) At the end of 100 µs, surface tension causes the bubble to collapse.

The efficiency of species formation of nanosecond pulse direct liquid phase discharge underlies the instantaneous conversion of water into plasma state. Produced species are converted back into liquid state and liquid interactions are more efficient in comparison to gas phase discharges interacting with liquids or traditional chemical methods [12, 37].

2.5 Chemical reactions in the discharge channel

Pulsed electrical discharges in or in contact with liquids induce conductive streamer channels and high energy electrons which are able to dissociate and ionize water molecules to radicals. Radicals are atoms or molecules with unpaired electrons at the valence band. Discharges in water form Reactive Oxygen Species (ROS). These are e.g. oxygen (O), hydroxyl (OH) and hydroperoxyl (HO_2) [38]. Once these highly reactive primary species are formed in the discharge channel, they react with each other to form secondary species like molecular oxygen (O_2), molecular hydrogen (H_2) and hydrogen peroxide (H_2O_2) or react with solutes in the bulk. As the discharge and its behavior is dependent on properties like applied voltage, electrode and liquid properties, these parameters highly affect the species formation. [39–44].

The overall stoichiometric ratio of molecular hydrogen, hydrogen peroxide and oxygen is of 4 : 2 : 1 [41] which is shown by reaction R 1:

$$6\,H_2O \longrightarrow 4\,H_2 + 2\,H_2O_2 + O_2\cdot \tag{R 1}$$

Water molecules are dissociated and ionized by the electrons to hydrogen (H_2) and hydroxyl (OH). Reaction R 2 is the main discharge reaction, M is a secondary reactant which can be H_2O. Oxygen (O) is formed as in reaction R 3. The discharge reactions occur during the pulse.

$$H_2O + M \longrightarrow H + OH + M \tag{R 2}$$

$$OH + OH \longrightarrow H_2O + O \tag{R 3}$$

After the pulse, the bubble expands and the primary species recombine to form secondary species. These reactions are:

$$OH + OH \longrightarrow H_2O_2 \tag{R 4}$$

$$O + O \longrightarrow O_2 \tag{R 5}$$

$$H + H \longrightarrow H_2 \tag{R 6}$$

$$H + O_2 \longrightarrow HO_2 \tag{R 7}$$

These reactions have described been more detailed in literature [13, 15, 45].

Medodovic and Locke [45] and Sahni et al. [46] conclude, that reaction R 4 is the major reaction for hydrogen peroxide formation. As two hydroxyl recombinate to hydrogen peroxide, the measurement of hydrogen peroxide concentration in a discharge system can give information about oxidation effects of the system. Hydrogen peroxide formation in a pin-to-plate configuration increases with increasing applied voltage and decreases with increasing solution conductivity [42, 47]. A modeling of the species creation for microsecond pulsed discharges in water has been performed by Medodovic and Locke [45].

3 Experimental Methods

The experimental methods will be described in this chapter. First, the water conductivity and absorption spectroscopy are explained. Then, the colorimetic method including the measuring process are addressed. At the end, the parameters of the performed measurements are given next to the concentration and error calculation.

3.1 Discharge setup

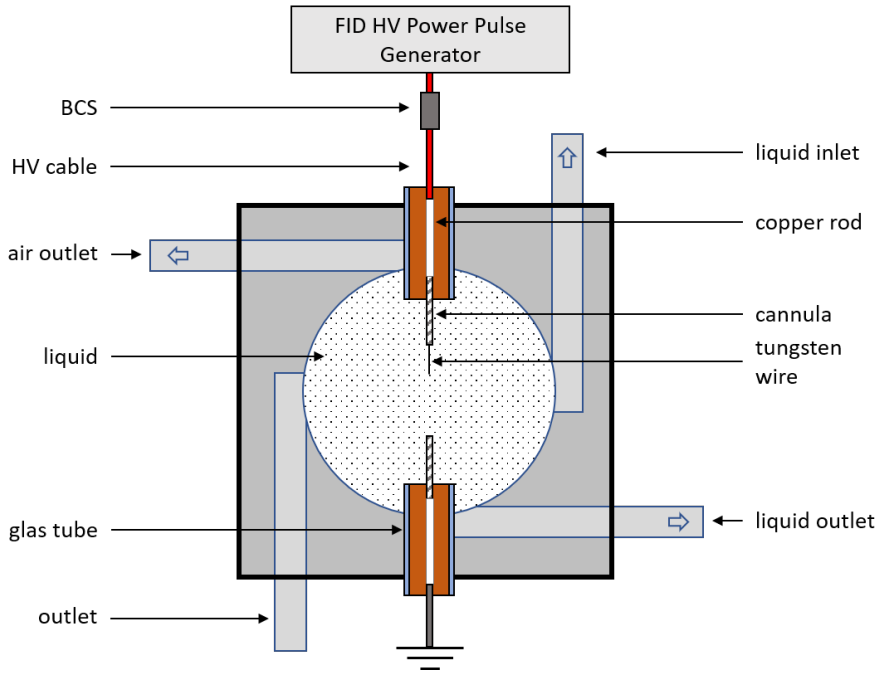

Figure 3.1: Discharge setup with a pin-to-pin electrode configuration.

The discharge chamber (fig. 3.1) is built in a pin-to-pin configuration with a volumetric capacity of 25 mL and it is made of Polymethylmethacrylat. The driven top electrode is a tungsten wire which is connected over a cannula, a glas shielded copper rod and high voltage cable to the power generator. The grounded electrode consists of a cannula made of stainless steel inserted into a glass surrounded copper rod and is placed at the bottom. The electrodes are placed in a distance of approximately 5 mm to 10 mm, depending on the wear of the tungsten wire.

A liquid inlet is placed on the side with the opening facing up and an outlet is positioned at the lowest point of the chamber. In addition an air outlet is mounted at the highest point. For all measurements distilled water with a conductivity of $2\,\mu S\,cm^{-1}$ was used.

The 50 µm thick tungsten wire yields high field strength at the tip and it is kept the same to ensure the equal condition during all measurements. The power generator is a FPG 30-01NK10 High Voltage Pulse Generator (FID GmbH). It generates 10 ns pulses with rise times of 2 ns to 3 ns within the frequencies between 1 Hz and 100 Hz of voltages in the range of 15 kV to 30 kV. A 11.95 m RG217 coaxial copper high voltage cable connects the electrode and the power generator. A back current shunt (BCS) for additional pulse monitoring is mounted into this cable. The whole setup is built in a Faraday cage for electromagnetic field shielding of measuring devices and for general risk reduction.

3.2 Water conductivity

For the production of hydrogen peroxide, the electric conductivity of the distilled water is important as described in section 2.5. On that account the electric conductivity is measured before and after the treatment with a conductivity meter GLF100 (GHM Messtechnik). No change in the conductivity of $\sigma = 2\,\mu S\,cm^{-1}$ is observed.

3.3 Absorption Spectroscopy

A common way to analyze treated water is by optical diagnostics. Within this method, absorption spectroscopy can determine the absorption spectrum of gases, liquids or solids as a function of wavelength by measuring the absorption of irradiation as it passes through the substance and interacts with it. H_2O_2 is difficult to detect directly due to its broad UV absorption spectrum [48, 49]. By using the colorimetric method, the detection of H_2O_2 can be enhanced. Therefore optical absorption spectroscopy can be performed.

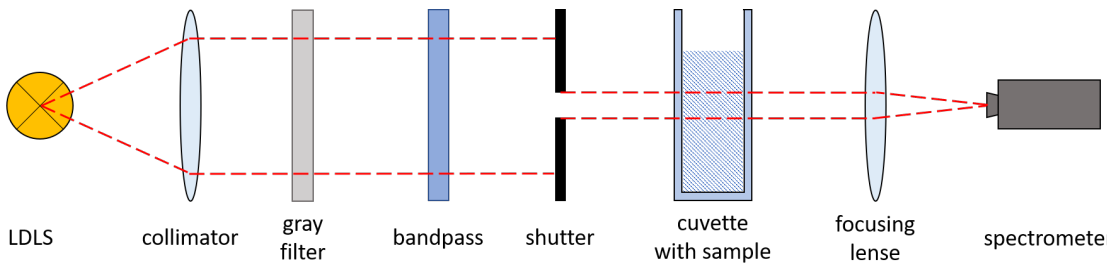

Figure 3.2: Optical absorption spectroscopy setup.

The optical absorption spectroscopy setup is shown in figure 3.2. It is designed in a one beam configuration. The light source is an EQ-99XFC LDLS™ (Energetiq Technology Inc.) which is a "Laser Driven Light Source" with a spectrum reaching from 190 nm to 2100 nm and a fiber-coupled output. To achieve a parallel light beam a collimating lens with a focal length of 60 mm is placed behind the glass fiber. A gray filter is used to attenuate the high intensity of the light beam that passes a 350 nm to 650 nm band-pass filter to eliminate unnecessary wavelengths and a shutter for a smaller light beam diameter. The beam then goes through the 10 mm

path length UV-Cuvette (BRAND®) filled with the sample. For a fixed and easy placing of the cuvette, a holder has been made out of stainless steel and mounted on a platform. A focusing lens with a focal length of 60 mm focuses the light beam to the glass fiber that is connected to a SILVER-Nova 25 TEC BW16 (StellarNet Inc.) spectrometer. The whole setup is built in an optical 30 mm cage system on an optical bench for better adjustments and alignments.

3.4 Colorimetric method

As mentioned above, H_2O_2 has a continuous absorption spectrum between 215 nm to 375 nm [48] and can be measured at 230 nm [49]. Generally, colorimetric method with titanium sulfate reagent is used to measure H_2O_2 [41, 44, 50]. This method was developed by Eisenberg in 1943 [51] and is able to detect H_2O_2 in the range of $2\,\mathrm{mg\,L^{-1}}$ to $30\,\mathrm{mg\,L^{-1}}$. However, this method requires a preparation of the titanium sulfate reagent with titanium dioxide and sulforic acid solution.

A more user friendly commercial test kit by Merck KGaG with the Neocuproine-Copper(II) method with a detection range matching the concentration of H_2O_2 found in the treated water was used in this work. H_2O_2 reduces Cu^{II} to Cu^{I} in presence of Neocuproine (NC). The overall stoichiometry can be seen in reaction 8. The color of the sample is yellow to orange with an absorption maximum at 454 nm. Tütem et al. [52] and Pecci et al. [53] have described this spectrophotometric determination of H_2O_2 in detail.

$$2\,Cu^{2+} + 4\,NC + H_2O_2 \longrightarrow 2\,Cu(NC)_2{}^{+} + O_2 + 2\,H^{+} \qquad \text{(R 8)}$$

The H_2O_2 test kit is the Spectroquant® Hydrogen Peroxide Test 1.18789.0001 (Merck KGaG). It contains one H_2O_2-1 reagent bottle with Cu^{II}-ions and another H_2O_2-2 reagent bottle with NC. Using a cuvette with 10 mm path length, the measuring range is within $0.03\,\mathrm{mg\,L^{-1}}$ to $6.00\,\mathrm{mg\,L^{-1}}$. If the cuvette is of 20 mm path length the measuring range will be more sensitive by a factor of two. For convenience purpose, the H_2O_2 concentration will be given in $\mu\mathrm{mol\,L^{-1}}$ at this point. Using the relation $n = m/M$ with the molar mass $M_{H_2O_2} = 34.0147\,\mathrm{g\,mol^{-1}}$, the measuring range equals $0.88\,\mu\mathrm{mol\,L^{-1}}$ to $176.39\,\mu\mathrm{mol\,L^{-1}}$. As the treated water has a pH of 5, it lies in the range of 4 to 6 required for the used of the kit.

3.4.1 Measuring process

The process of treatment and H_2O_2 measurement is described in the following:

For every measurement new distilled water needs to be filled in the chamber. With the air outlet opened, a constant but high water flow through the liquid inlet leads to a small air bubble or even no air bubble in the chamber. This will guarantee the same amount of water of 25 mL throughout the experiment. As the chemical reaction during the discharge is not depending on the water amount, latter could affect the H_2O_2 concentration in its consecutive determination. Once the chamber

is filled, the HV pulser can be turned on.

To determine the H_2O_2 concentration in the liquid, 0.5 mL of reagent H_2O_2-1 of the test kit needs to be pipetted into a test tube. Then, 8.0 mL of the treated water can be added and mixed. Finally, 0.5 mL of reagent H_2O_2-2 has to be pipetted into the test tube and mixed. After 10 min reaction time, the sample can be filled in the cuvette and can be measured with the optical absorption spectrometer.

Before using the spectrometer, the light source needs to be turned on at least 20 min in prior for stable light. Due to the frequently crashing software of the spectrometer, the transmittance or "scope mode" is used and the spectra are saved as text files. The absorbance is calculated by post treatment of the data with a self-written python script. The attenuation of the intensity of the light by passing the treated water with the reagent follows the Beer-Lambert Law:

$$A = -log_{10}\Big(\frac{I_1}{I_o}\Big) = \epsilon cd. \tag{3.1}$$

The absorption is A. The reference spectrum is I_0 which is the reagent used on untreated water. The spectrum of the treated sample is I_1, ϵ is the molar extinction coefficient, c is the concentration and d is the path length of the light. For each set of measurements the reference needs to be made and its spectrum needs to be measured. This will ensure the elimination of changes at the spectrometer and variation of water and reagent absorption is taken into account each time to minimize the error of the measurement. Both intensities I_0 and I_1 need to be subtracted by the dark spectrum I_{dark} due to the background noise of the spectrometer. Therefore, I_{dark} is also needed.

3.4.2 Calibration

The calibration of the absorption spectrometer is achieved by diluting a commercial H_2O_2 standard 30% solution with distilled water to the detection range of the test kit. The molar concentration of the H_2O_2 standard 30% solution is $9.8075\,\text{mol}\,\text{L}^{-1}$ and the density of $1.112\,\text{g}\,\text{mL}^{-1}$ at 20 °C.

Two calibrations are performed with the first test kit used for all measurements (fig. 3.3) and a new second test kit right after all measurements (fig. 3.4). The absorption value A as a function of known hydrogen peroxide concentration c with the hydrogen peroxide test kits are shown.

The calibration with the first test kit will be used to calculate the H_2O_2 concentration for the results. The calibration with the second kit will not be used as it does not show a linear behavior until the maximum detection range. A detailed discussion about the calibration can be found in section 4.1. To calculate the concentration c of the sample, the molar extinction coefficient ϵ is needed.

The linear fit with the equation (3.2):

$$A = \epsilon cd + A_0, \tag{3.2}$$

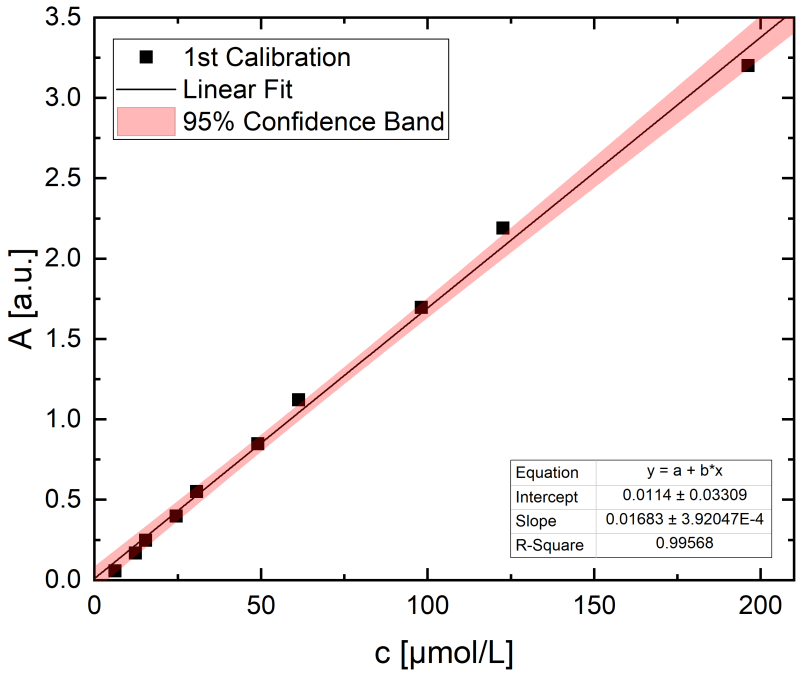

Figure 3.3: Calibration curve 1: Absorption value A as a function of known hydrogen peroxide concentration c with the first hydrogen peroxide test kit. This kit was used for the measurements with time, frequency and voltage variation.

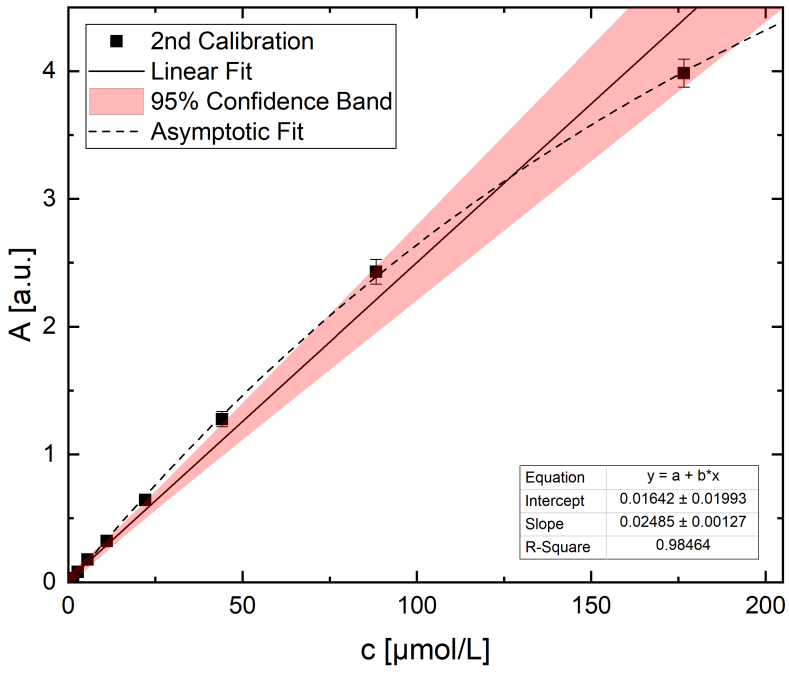

Figure 3.4: Calibration curve 2: Absorption value A as a function of known hydrogen peroxide concentration c with the second hydrogen peroxide test kit. This kit is a "new" test kit.

with A_0 denoting the y-intercept and $d = 1\,\mathrm{cm}$ is the path-length of the cuvette,

yields

$$\epsilon_1 = (0.0168 \pm 0.0004)\,\mathrm{L\,\mu mol^{-1}\,cm^{-1}}, \quad A_{0,1} = (0.01 \pm 0.03)\,\mathrm{a.u.} \tag{3.3}$$

and

$$\epsilon_2 = (0.0249 \pm 0.0013)\,\mathrm{L\,\mu mol^{-1}\,cm^{-1}}, \quad A_{0,2} = (0.02 \pm 0.02)\,\mathrm{a.u.}. \tag{3.4}$$

3.5 Performed measurements

In order to analyze the hydrogen peroxide production in this nanosecond pulsed discharge in water, measurements of the hydrogen peroxide concentration with variation of different parameters were performed. These measurements are time (1), frequency (2) and voltage (3) variations and the different parameters can be seen in table 3.1. Chosen parameters will be discussed in the result section 4.2.

Table 3.1: Parameters of the measurements to analyze the behavior of the hydrogen peroxide production.

Parameter: / Measurement:	time t [min]	frequency f [Hz]	voltage U_{HV} [kV]
time (1)	3; 5; 10; 20	15	20
frequency (2)	5	1; 15; 30; 60; 100	20
voltage (3)	10	15	15 - 30

3.6 Concentration and error calculation

The hydrogen peroxide concentration c_m of the measurements with different treatment time, frequency and voltage and its error Δc_m is calculated as

$$c_m = \frac{A_m - A_0}{\epsilon d} \tag{3.5}$$

and

$$\begin{aligned} \Delta c_m &= \left|\frac{\delta c_m}{\delta A_m}\right| \Delta A_m + \left|\frac{\delta c_m}{\delta A_0}\right| \Delta A_0 + \left|\frac{\delta c_m}{\delta \epsilon}\right| \Delta \epsilon \\ &= \left|\frac{1}{\epsilon d}\right| \Delta A_m + \left|-\frac{1}{\epsilon d}\right| \Delta A_0 + \left|-\frac{A_m - A_0}{\epsilon^2 d}\right| \Delta \epsilon, \end{aligned} \tag{3.6}$$

where A_m represents the mean absorption value of the measurements and ΔA_m is the standard deviation of the mean. The error of the path length d is small enough to be neglected. Errors that occur during the calibration and measurements are difficult to determine because of the procedure. The errors of the parameters are given indirectly by the variation of the H_2O_2 standard solution concentration, the changing ambient temperature and pressure, the use of pipettes and the minimal technical error during the measurements process. To account these errors, the estimate of the largest error is used instead of the Gaussian error propagation.

4 Results

In this chapter, the performed study are analyzed and discussed. First, the discussion of the calibration is given before the results of the influence of the parameters on the hydrogen peroxide concentration are evaluated. Then, an estimation of the initial temperature based on the cavitation theory is performed. Next, the Global Kinetic Model is introduced and the calculation is presented. At the end, the consideration of quantum plasma is analyzed.

4.1 Calibration discussion

Based on the calibration, all concentrations will be calculated. Therefore, errors of the calibration will be discussed in detail. The first calibration line (see. fig 3.3) was obtained with the same test kit used for all measurements. Only one set of measurements is performed. This explains the absence of y-errors. The second calibration line (see fig. 3.4) has been performed with the second test kit of the same charge as the first test kit but it does not show a linear behavior for the full detection range from $0.88\,\mu mol\,L^{-1}$ to $176.39\,\mu mol\,L^{-1}$, which can be seen if comparing the linear and the asymptotic fit. Instead, the saturation starts at approximately $120\,\mu mol\,L^{-1}$, which yields a 48 % higher molar extinction coefficient compared to the first calibration line. For both, the same H_2O_2 solution was used. Since the first calibration line is not of triplicate, in comparison to the second calibration line, statistical errors during the process which could occur e.g. while using pipettes cannot be excluded. Triplicate measurements have been made for the second calibration curve using the Eppendorf Multipette® M4.

To exclude possible statistical errors caused by the latter, another calibration with the second test kit using manual pipettes was executed, which shows results with the same behavior as the second calibration line (no graphic included). Therefore, errors during the process or caused by the instruments are unlikely to have appeared. Density and concentration changes of the H_2O_2 standard solution due to pressure and temperature fluctuations can be neglected because changes of these ambient parameters were not sufficient to influence the density and the concentration of the H_2O_2. Since both test kits are of the same charge, three possible cases can be conducted to explain the differences. First, experimental and instrumental errors were made in the first calibration, which cannot be determined afterwards as the kit is empty. Second, the first test kit oxidizes while in contact with air during the measurements even if the flask was closed immediately. Third, the test kits are of different molar extinction coefficients due to concentration inconsistencies during the production process. It is most likely that the second case causes the difference in the calibration curve due to the long measurement process for this thesis. Nonetheless, the first calibration line will be used for further calculation as this test kit was

used for the measurements.

4.2 Influence of the parameters on the hydrogen peroxide concentration

The analyze of the influence of the parameters on the hydrogen peroxide concentration are examined by treatment time, frequency and voltage variation. In addition, the influence of the electrode gap distance is investigated.

4.2.1 Treatment time variation

Measurements of the H_2O_2 concentration with treatment times of 3 min, 5 min and 20 min have been performed at a voltage U of 20 kV at a frequency f of 15 Hz to evaluate concentration changes (fig. 4.1). As discussed in section 2.2, each discharge and breakdown initiates formation of primary and product species. The most stable product besides water and molecular oxygen is hydrogen peroxide. With increasing treatment time, more discharges occur with similar discharge properties. This should give a linear increase of the hydrogen peroxide concentration as shown in literature [41, 43].

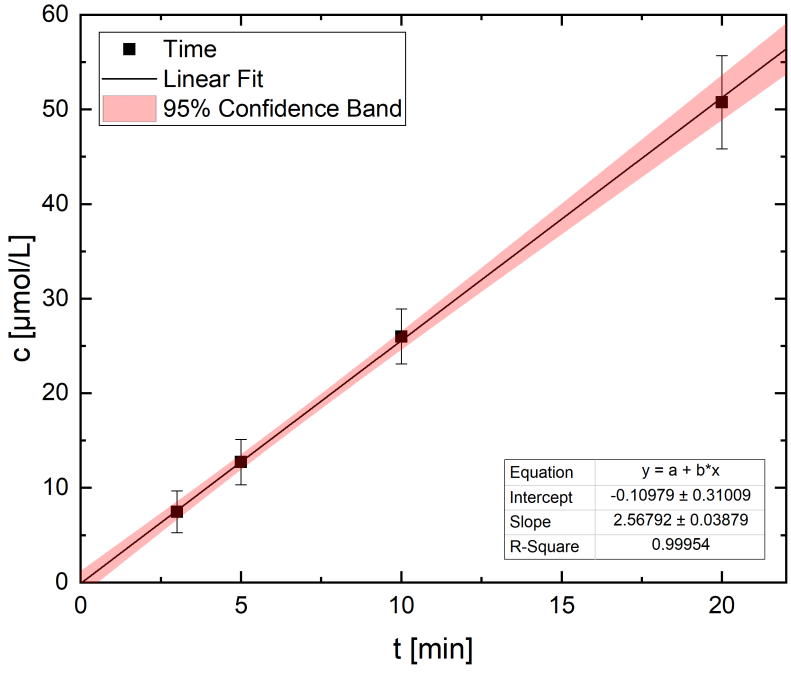

Figure 4.1: Hydrogen peroxide concentration c as a function of treatment time t at $U = 20$ kV and $f = 15$ Hz.

Regarding to this, the chosen treatment time was set to a maximum of 20 min because a saturation cannot be reached. Even after hours of treatment time as the production of species will increase linearly until few water molecules are left. The

amount of water molecules in the estimated initial radius of the volume $r_0 = 25\,\mu m$ is about 3.6 nmol, compared to the water inside the discharge chamber with a volume of 25 mL, which is about 1.38 mol. Additionally, not all of the water inside the initial radius can be converted into hydrogen peroxide. The aspect of efficiency will be discussed later. The voltage of 20 kV at the frequency of 15 Hz has been chosen because this parameter shows a H_2O_2 concentration that is in a good measuring range of the H_2O_2 test kit. Higher parameters show the same correlation between the concentration and the different treatment time.

As assumed, figure 4.1 clearly shows a linear increase of the H_2O_2 production. The linear regression results in the slope m_t and intercept b_t of

$$m_t = (2.57 \pm 0.04)\,\mu mol\,L^{-1}\,min^{-1}, \quad b_t = (-0.1 \pm 0.3)\,\mu mol\,L^{-1}. \tag{4.1}$$

The hydrogen peroxide concentration as a function of the treatment time at the voltage of 20 kV at the frequency of 15 Hz increases by the factor m_t. For $t = 0$ min, the concentration should be 0, which is in the error range of the intercept b_t.

4.2.2 Frequency variation

An increase in discharge frequency is expected to lead to a linear increase of the H_2O_2 concentration. This is valid as long as the frequency is not high enough to ignite within the duration of the previous discharge since it is assumed that each ignition takes place in "new" water. The estimate of the entire discharge duration until the bubble collapses is $t_{bubble} = 100\,\mu s$ [12].

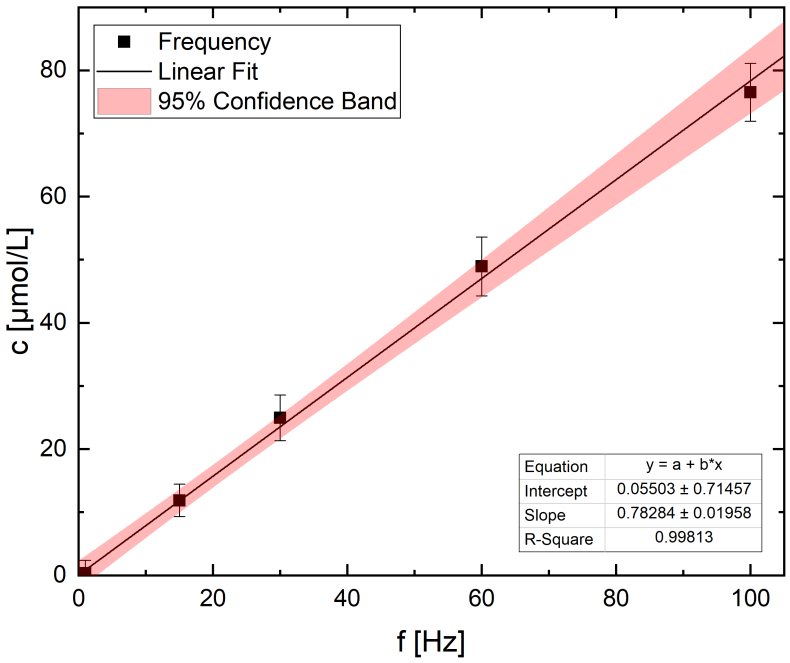

Figure 4.2: Hydrogen peroxide concentration c as a function of discharge frequency f at $U = 20$ kV and $t = 5$ min.

The highest possible frequency of the HV pulser is $f_{max} = 100$ Hz, which leads to a discharge every 10 ms. In comparison to the duration of the pulse of $t_{pulse} = 10$ ns,

the time between each pulse is in the order of the magnitude 10^2 higher than t_{bubble}. Therefore, the linear behavior should still be valid for f_{max}. Thermal changes of the liquid by the discharge are quickly compensated and can be neglected, as the estimated initial radius of the volume is $r_0 = 25\,\mu\text{m}$, which results in a volume of $65 \times 10^{-15}\,\text{m}^3$, in comparison to the 25 mL=$2.5 \times 10^{-5}\,\text{m}^3$. Furthermore, the expansion of the bubble is adiabatic.

Figure 4.2 depicts the H_2O_2 concentration as a function to the treatment frequency at the voltage $U_{\text{H}} = 20\,\text{kV}$ and the treatment time of $t = 5\,\text{min}$. The treatment time of 5 min has been chosen in consideration of the wear of the electrode to not stress the electrode for too long as the tip will shorten quickly in the high frequency range. The linear regression results in the slope m_{f} and intercept b_{f} of

$$m_{\text{f}} = (0.783 \pm 0.020)\,\mu\text{mol}\,\text{L}^{-1}\,\text{Hz}^{-1}, \quad b_{\text{f}} = (0.1 \pm 0.7)\,\mu\text{mol}\,\text{L}^{-1}. \tag{4.2}$$

This finding confirms the assumption of the linear increase of the H_2O_2 concentration with increasing discharge frequency of the factor m_{f} at the voltage $U_{\text{H}} = 20\,\text{kV}$ and the treatment time of $t = 5\,\text{min}$. For $f = 0\,\text{Hz}$, no discharge can produce hydrogen peroxide. This liess in the result of the given intercept b_{f}.

4.2.3 Voltage variation

In comparison to the parameter variation of time and frequency, the voltage has a major influence on the discharge. The initial pressure p_0 and volume V_0 depend on the energy E_0 dissipated into the liquid according to cavitation theory [12]. This means that the energy going into the microbubble and streamer creation is higher with increasing voltage U_{HV}, which is linked to a higher temperature. Due to the non-thermal behavior of the plasma, the term temperature has to be used with care. Nevertheless, higher temperature result in higher dissociation and ionization rate of the water molecules. An increase of the voltage will therefore increase the H_2O_2 production. Based on the correlation $p_0 \propto U_{\text{HV}}^2$ [12] (see fig. 2.3), the H_2O_2 production rate should decrease for higher voltages.

Measurements to verify this assumption have been made in the voltage range of 15 kV to 30 kV at $f = 15\,\text{Hz}$ and $t = 10\,\text{min}$ treatment time (fig. 4.3). The discharge ignition in distilled water of $\sigma = 2\,\mu\text{S}\,\text{cm}^{-1}$ was irregular under 15 kV. The H_2O_2 concentration increases quickly until approximately 21 kV which correlates to $32\,\mu\text{mol}\,\text{L}^{-1}$, before it starts to decline and saturate. The hydrogen peroxide production is strongly dependent in the initial temperature, which is linked to the initial pressure. Hence, a decline of the hydrogen peroxide production rate should be seen for increasing voltage. This is confirmed by the result of the measurement.

The optimal voltage range with the maximum H_2O_2 production rate of $37\,\mu\text{mol}\,\text{L}^{-1}$ at 21 kV for 15 Hz and 10 min treatment time is right in the voltage range of the HV pulser from 15 kV to 30 kV. This voltage can be considered as the optimum voltage for the H_2O_2 production.

The large error bars in figure 4.3 result from the five sets of measurements and the error of the calibration. Within one set, the H_2O_2 concentration is measured

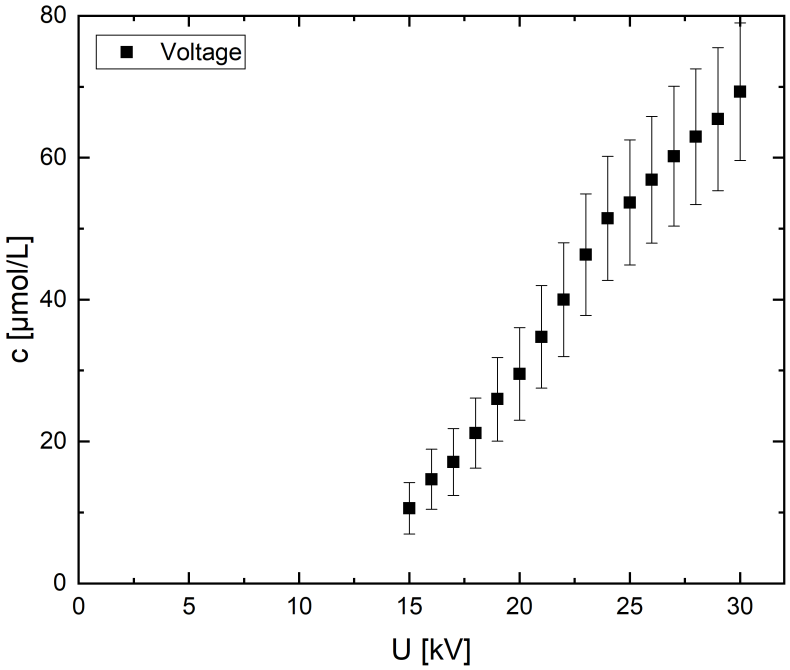

Figure 4.3: Hydrogen peroxide concentration c as a function of discharge voltage U at $f = 15\,\mathrm{Hz}$ and $t = 10\,\mathrm{min}$.

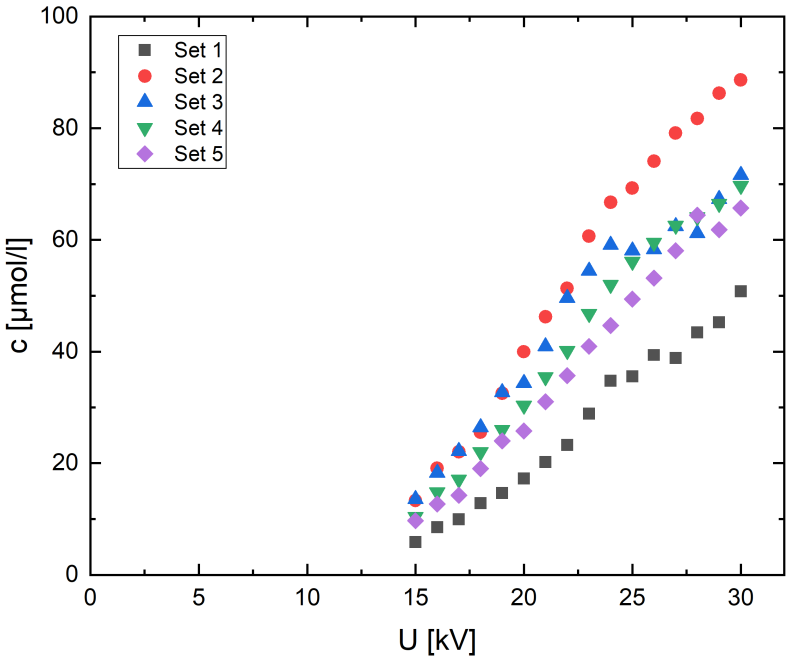

Figure 4.4: Sets of the hydrogen peroxide concentration c as a function of voltage U at $f = 15\,\mathrm{Hz}$ and $t = 10\,\mathrm{min}$.

from 15 kV to 30 kV. After each set, the H_2O_2 concentration decreases proportionally (see. fig. 4.4). Set 1 may be an outlier. Ambient temperature, pressure, conductivity changes are small and negligible as their influences on the water and discharge are not sufficient. No changes in the setup or in the measurement process have been

made.

Possible errors for this are the increase of the electrode gap due to wear of the tip (see. section 4.2.4) and the minimal changes in H_2O_2 test kit if it gets in contact with air. The observation is that the Neocuproine (NC) solution in the H_2O_2-2 reagent bottle oxidizes quickly when exposed to air. This could change the concentration of the H_2O_2 test kit and the ratio of the Cu^{II} to the NC is changed when mixed with the treated water in the test tube. The absorbance of the latter would change. Since the oxidation accumulates during the measurements as the bottle will be exposed to the air, the absorbance and therefore the H_2O_2 concentration could decrease accumulatively with the number of sets of measurements.

4.2.4 Electrode distance

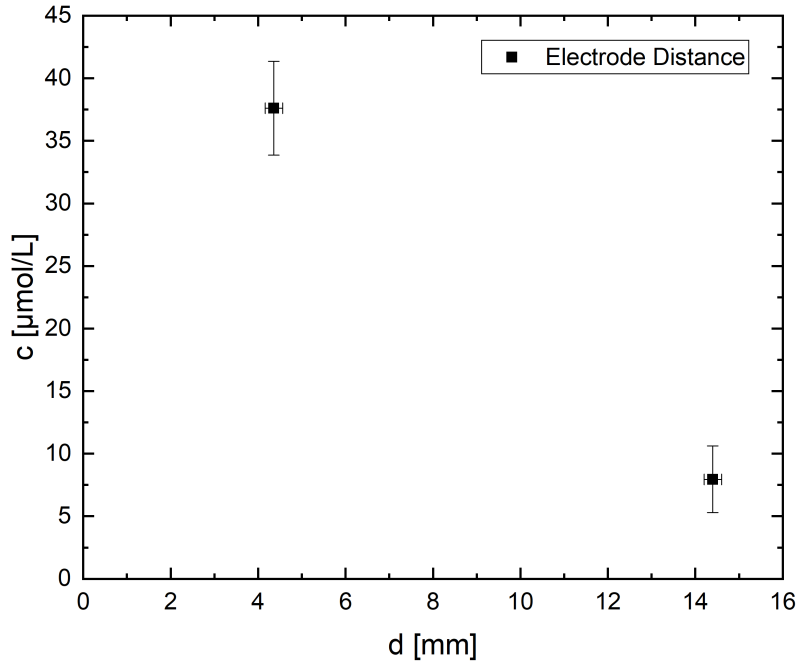

Figure 4.5: Hydrogen peroxide concentration c in dependency to the electrode distance d at $U = 20\,\mathrm{kV}$ and $f = 15\,\mathrm{Hz}$.

For the evaluation of the H_2O_2 concentration dependency on the electrode distance as mentioned earlier, measurements of the H_2O_2 concentration in dependency of two electrode distances at $U = 20\,\mathrm{kV}$ and $f = 15\,\mathrm{Hz}$ have been realized (see fig. 4.5). The distance of the electrodes was determined by a digital camera imaging and a reference length in the picture. It can be seen that the H_2O_2 concentration is approximately 81 % lower if the distance increases by a factor of 3.5. One possible explanation is the increase of the resistance $R = U/I$ and decrease of the current I if the distance between the electrodes increases. This is due to the calculation of the resistance with the Pouillet's law

$$R = \rho \frac{l}{A}, \tag{4.3}$$

where l denotes the distance between the electrodes, ρ is the electrical resistivity and A is the cross section area.

In respect to the electrical field E at the tip, which is of $\mathrm{MV\,cm^{-1}}$ [54], an increase in the distance d lowers E as

$$E = -\frac{U}{d}. \tag{4.4}$$

These explanations are supported by the observation of the brightness of the discharge. For a small electrode gap, the discharge is brighter, hence the current I, the temperature T and the electric field E are higher, thus greater H_2O_2 production in comparison to a big gap.

4.3 Temperature estimation based on the cavitation theory

In consideration of the cavitation theory by Grosse et al. [12], the potential energy E_0 which drives the bubble expansion is expressed in $E_0 = p_{0,gas}V_0$. As V_0 is of the constant radius $r_0 = 25\,\mu\mathrm{m}$, the initial pressure $p_{0,gas}$ can be expressed as a function of the discharge voltage U (fig. 2.3). In this thesis the initial pressure $p_{0,gas}$ is p_0. Due to the inertia of the liquid, the initial number of species N_0 in V_0 must be constant. Hence, the potential energy is equal to $E_0 = N_0 k_\mathrm{b} T_0$. The initial temperature T_0 can be calculated as in equation (4.5), which is equal to the ideal gas law.

$$T_0 = \frac{p_{0,gas}V_0}{N_0 k_\mathrm{b}} \tag{4.5}$$

k_b is the Boltzmann constant, $V_0 \approx 65 \times 10^{-15}\,\mathrm{m^{-3}}$ is calculated using the initial radius of $r_0 = 25\,\mu\mathrm{m}$ and $N_0 \approx 2 \times 10^{15}$ with the water density of $\rho = 997\,\mathrm{kg\,m^{-3}}$ at 20 °C and 1 atm and the molar mass of $M = 18.015\,\mathrm{g\,mol^{-1}}$. The fitting for continuous expression of the calculated initial pressure $p_{0,gas}$ as a function of the voltage U by the cavitation theory can be seen in figure 4.6. Exponential fitting methods have been tested but the polynomial fit in order of 2 shows the best shape for these few data points of voltages 14 kV, 18 kV, 22 kV and 24 kV. According to the deduced scaling of $p_\mathrm{initial} \propto U^2$ [12] (see fig. 2.3), the same scaling for the initial pressure p_0 will be made at this point and a quadratic fit is preferred.

Based on the cavitation theory, the initial temperature T_0 can be derived with the assumption of the ideal gas law (see. eq. 4.5) with constant initial volume V_0 and initial number of species N_0. To get an impression of the temperature dependence of this chemical reaction the decomposition of hydrogen peroxide can be considered (see. R 9).

$$\mathrm{H_2O_2} \longrightarrow \mathrm{H_2O} + \frac{1}{2}\,\mathrm{O_2} \tag{R 9}$$

The standard Gibbs free energy of formation $\Delta G_\mathrm{f}\circ$ of this reaction is $-120.42\,\mathrm{kJ\,mol^{-1}}$ [55], which is equivalent to approximately 1.2 eV or 14 000 K. The standard Gibbs free energy of formation of a chemical compound describes the change of the Gibbs free energy, which is required to form 1 mol of the substance of the elements its consists of. This energy defines the equilibrium criterion at constant temperature when the thermodynamic potential is at minimum. Raising the energy in the system above this energy will shift the equilibrium to the product direction. If the energy is

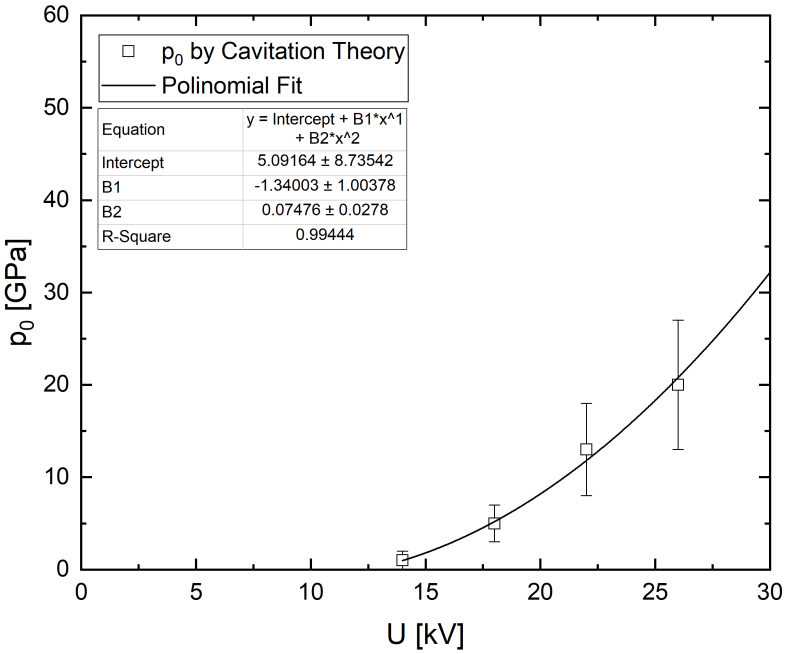

Figure 4.6: Quadratic fitting of the pressure p_0 inside the initial bubble with radius of 25 µm as a function of discharge voltage U to model the expansion of the cavitation bubble [12].

below, the reaction will shift to the reactant direction. Detailed information can be found in literature [56]. In this case, water and molecular oxygen will form hydrogen peroxide if the energy in the system is above 14 000 K. Plotting reaction 9 in figure 4.7 according to the Arrhenius equation, the reaction rate k is

$$k \approx Ae^{-14\,000\,\mathrm{K}\,T^{-1}}. \tag{4.6}$$

The pre-exponential factor A is set to $10^{1.9}$ for the best fit.

The H_2O_2 concentration as a function of the initial temperature can be seen in figure 4.7. High initial temperatures up to 70 000 K are caused by the initial temperature estimation based on the cavitation theory described above. The initial pressure $p_{0,gas}$ and V_0 from cavitation theory show a good prediction for the bubble expansion observed by shadowgraphy and schlieren imaging [12]. Hence, the same assumption is used to calculate T_0 in V_0 and the resulting initial number of species in N_0 in this sphere. The potential energy is $E_0 = p_0 V_0$. If the initial volume V_0 is smaller than assumed, the initial pressure p_0 will increase. Regarding to the ideal gas law (see eq. 4.5), the initial temperature T_0 would rise due to the smaller amount of species $N_0 \propto r_0^3$ in the volume. Even if N_0 would change, the impact of this parameter on the initial temperature calculation is not sufficient because of the high initial pressure in the GPa range. As a conclusion for the analysis of T_0, the assumption of the ideal gas law and the constant V_0 and N_0 has a major impact on the result and is therefore the main weakness of this estimation. In comparison to the Arrhenius equation, however, the overall trend of the H_2O_2 concentration can be seen as a temperature depending chemical reaction of Arrhenius type (see. fig 4.7). The difference of the measurements to the Arrhenius plot results from the simplified

assumption for the Arrhenius equation.

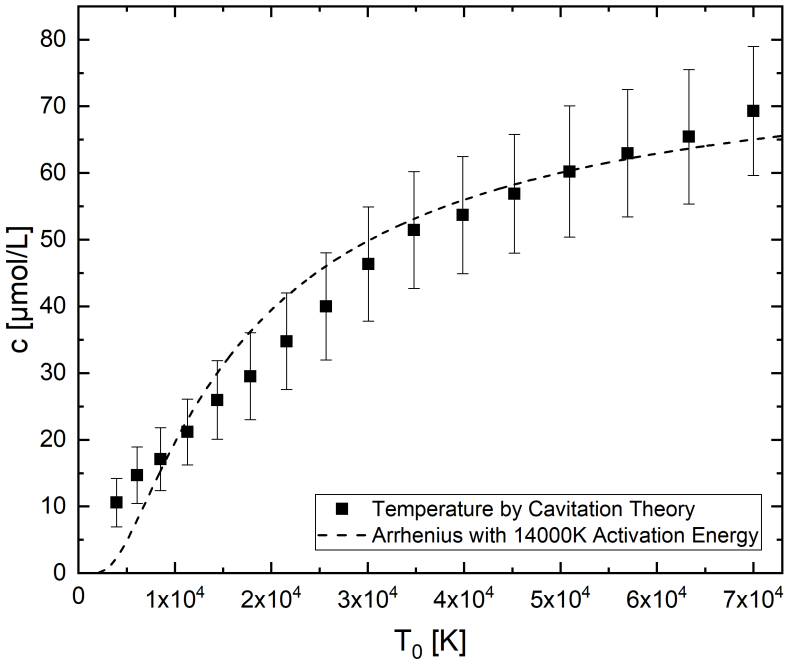

Figure 4.7: The solid symbols is the H_2O_2 concentration c as a function of the initial temperature T_0 derived from the potential energy by the cavitation theory with constant V_0 and N_0. The Arrhenius equation with the activation energy of 14 000 K is the dashed line.

To evaluate the evolution of the hydrogen peroxide during the discharge and by taking into account the adiabatic expansion of the bubble, a Global Chemistry Model based on the core and recombination model by Medodovic and Locke [45] will be used. During the pulse of 10 ns, nanopores and cavitation bubble with high temperatures and pressures are formed. Inside these nanopores, the water is dissociated and ionized completely and reaches super critical state. After the pulse, the bubble expands adiabatically and the temperature drops. These two phases, which are the steps (a) to (b) and step (c) to (g) in figure 2.4, can be seen as the core model and the recombination model.

4.4 Global Kinetic Model

The Global Kinetic Model (GKM) is based on the core and recombination model by Medodovic and Locke [45] which they used for determination of the primary chemical reactions in a pulsed discharge in water. Formation of hydrogen (H), molecular hydrogen (H_2), oxygen (O), molecular oxygen (O_2), hydroxide (OH) and water during the core model within the pulse duration is the starting point for the recombination phase, which forms, among others, hydrogen peroxide. In contrast to the original model, both parts, the core model and the recombination model, are combined for the modeling in this thesis, thus reactions for the core and recombination model are

valid for the entire modeling time t_m of 10 µs. The duration of the bubble expansion process until its collapse is assumed to be $t_\mathrm{bubble} = 100\,\mu\mathrm{s}$ [12]. As t_bubble also includes the collapse of the bubble, the modeling time t_m is set before the collapse of the bubble. Once the bubble collapses, the produces species are mixed with the liquid bulk.

The modeling during the bubble expansion takes the assumptions of the cavitation theory by Grosse et al. [12] as starting point. These are (1) the density of the fully ionized water $n_0 = 3 \times 10^{22}\,\mathrm{cm}^{-3}$ at a pressure of $p_0 = 1\,\mathrm{GPa}$ and (2) the expansion velocity of the bubble, which is expressed by the decreasing scale of the density *n scale* and the temperature T. The starting point for the temperature T is the estimated initial temperature T_0 in section 4.3. The adiabatic expansion has been calculated in the cavitation theory and is expressed in the result of the pressure and temperature.

The density scaling *n scale* as a function of the time has been calculated as

$$n\,scale(t) = \frac{p_\mathrm{cav}(t)}{T_\mathrm{cav}(t)} \cdot \frac{T_\mathrm{cav,0}}{p_\mathrm{cav,0}}. \tag{4.7}$$

T_cav is the evolution of the temperature and p_cav is the evolution of the pressure evaluated with the cavitation theory. An example of the calculation can be seen in figure 2.2. $T_\mathrm{cav,0}$ and $p_\mathrm{cav,0}$ are the initial values. Furthermore, the temperature T as a function of the time is calculated as

$$T(t) = \frac{T_\mathrm{cav}(t)}{T_\mathrm{cav,0}} \cdot T_0. \tag{4.8}$$

T_0 is the initial temperature derived in section 4.3.

No geometrical dimensions of the bubble expansion are taken into account. Only the decline of *n scale* and T point out the adiabatic expansion of the bubble. Hence, the starting point is the number of water species $n_{\mathrm{H_2O},0} = 3 \times 10^{22}$ within a standard volume on $1\,\mathrm{cm}^3$. This results in plots of number of species n_s, temperature T and *n scale* as a function of the time ranging from $1 \times 10^{-10}\,\mathrm{s}$ to $1 \times 10^{-5}\,\mathrm{s}$. For $t = 0\,\mathrm{s}$, only water is present. Consequently, the modeling starts at $t = 1 \times 10^{-10}\,\mathrm{s}$. The examined species are H_2O_2, OH, H, O, H_2, O_2, H_2O_2 and HO_2. n_s is obtained by subtraction if the species are reactants and addition if they are products over the modeling time t_m. Moreover, no diffusion of the species is assumed as in [45] because of no participation in the reactions. After one discharge, the produced species distribute in the liquid and the next discharge occurs only in water without prior produced species.

The primary reactions used for the GKM are listed in table 4.1 with the rate constants k and the temperature range in which the different reactions are valid. Except molecular oxygen, these reactions form highly reactive species, which react with each other to form secondary stable products like water and hydrogen peroxide. Table 4.2 lists the secondary reactions used for the GKM. They are taken from the NIST Chemical Kinetic Database [57] and are adopted from [45].

The calculation of the reactions for the GKM is the multiplication of the $n\,scale^2$, the number of the reactant species n_s and the rate constant k. Some reactions

Table 4.1: List of primary reactions used for the Global Kinetic Model (M=H_2O, τ=(T/298)) [57], adopted from [45].

Reaction number	Reactions	Temperatur [K]	Rate constant [cm^{-3} $molecule^{-1}$ s^{-1}]
R 2.1	$H_2O + M \longrightarrow H + OH + M$	2000-6000	$5.8 \times 10^{-9} \exp^{-440\,kJ/RT}$
R 2.2	$OH + M \longrightarrow H + O + M$	300-2500	$4.09 \times 10^{-9} \exp^{-416\,kJ/RT}$
R 2.3	$H_2 + M \longrightarrow H + H + M$	2500-8000	$1.5 \times 10^{-9} \exp^{-402\,kJ/RT}$
R 2.4	$O_2 + M \longrightarrow O + O + M$	2000-10000	$1.99 \times 10^{-10} \exp^{-9.5\,kJ/RT}$
R 2.5	$OH + OH \longrightarrow H_2O + O$	250-3000	$1.02 \times 10^{-12} \tau^{1.4} \exp^{1.66\,kJ/RT}$

used for the core model have been excluded for the primary reactions as they have been taken into account in the secondary reactions. Although the maximum valid temperature is 10 000 K. This model still assumes their validity, because of good agreement with the experimental data observed in [45]. Medodovic and Locke assumed temperature ranges of 5000 K to 2000 K for the core model and 2000 K to 300 K for the recombination model. Nonetheless, there are no reports about rate constants in higher temperature range.

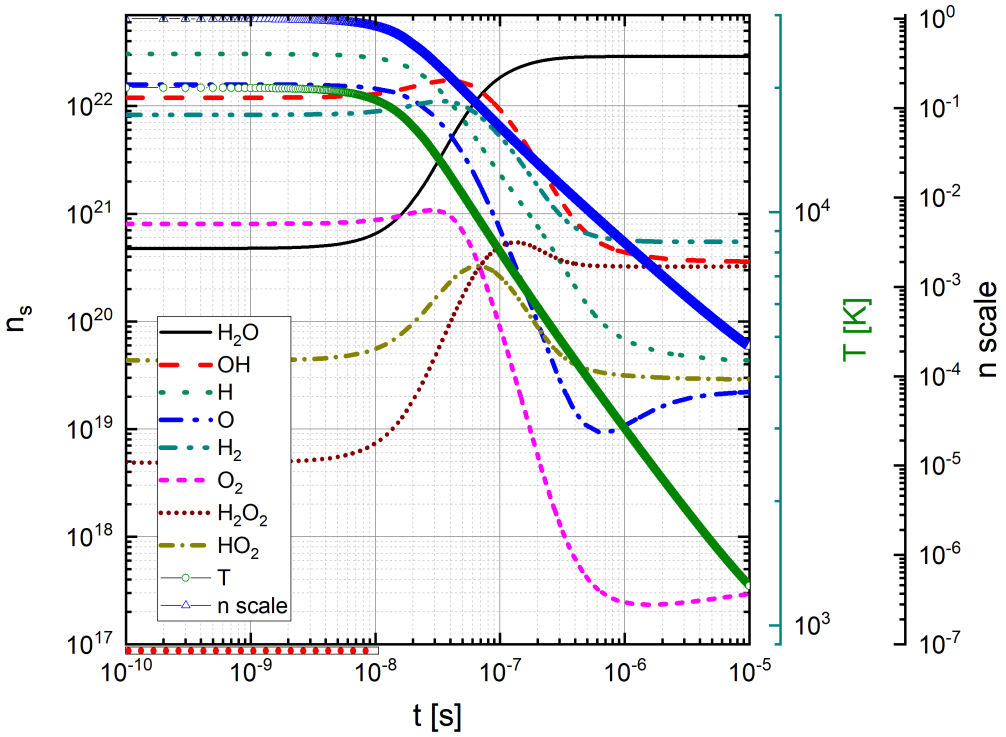

Figure 4.8: Number of species n_s, temperature T and density scale n *scale* for one discharge of the modeling time t_m as a function of time t. The initial temperature is $T_0 = 20\,000$ K. The initial pressure is $p_0 = 1$ GPa and the initial number of species is $n_{s,0} = n_{H_2O,0} = 3 \times 10^{22}$. The pulse duration is $t_{pulse} = 10$ ns (sparse area).

Figure 4.8 shows the number of species n_s, the temperature T and the density scale n *scale* for one discharge of the modeling time t_m as a function of time t.

Table 4.2: List of secondary reactions used for the Global Kinetic Model (M=H_2O, τ=(T/298)) [57], adopted from [45].

Reaction number	Reactions	Temperatur [K]	Rate constant [cm^{-3} $molecule^{-1}$ s^{-1}]
OH			
R 3.1	$O + OH \longrightarrow O_2 + H$	250-5000	$4.55 \times 10^{-12} \tau^{0.4} \exp^{3.09\,kJ/RT}$
R 3.2	$OH + H \longrightarrow H_2O$	300-2100	$2.69 \times 10^{-10} \exp^{-0.62\,kJ/RT}$
R 3.3	$H + OH \longrightarrow O + H_2$	300-2500	$6.86 \times 10^{-14} \tau^{2.8} \exp^{-16.21\,kJ/RT}$
R 3.4	$H_2O_2 + OH \longrightarrow HO_2 + H_2O$	300-2500	$2.91 \times 10^{-12} \exp^{-1.33\,kJ/RT}$
R 3.5	$O_2 + OH \longrightarrow HO_2 + O$	300-2500	$3.7 \times 10^{-11} \exp^{-220\,kJ/RT}$
R 3.6	$OH + OH \longrightarrow H_2O_2$	200-1500	$1.51 \times 10^{-11} \tau^{-0.37}$
R 3.7	$OH + OH \longrightarrow 2\,O + 2\,H$	300-2500	$4.09 \times 10^{-9} \exp^{-416\,kJ/RT}$
H_2O_2			
R 3.8	$H_2O_2 + O \longrightarrow HO_2 + OH$	300-2500	$1.42 \times 10^{-12} \tau^{2} \exp^{-16.631\,kJ/RT}$
R 3.9	$H_2O_2 + H \longrightarrow OH - H_2O$	300-2500	$4.01 \times 10^{-11} \exp^{16.63\,kJ/RT}$
R 3.10	$H_2O_2 + H \longrightarrow HO_2 + H_2$	300-2500	$8 \times 10^{-11} \exp^{-33.26\,kJ/RT}$
R 3.11	$H_2O_2 + O_2 \longrightarrow 2\,HO_2$	300-2500	$9 \times 10^{-11} \exp^{-166\,kJ/RT}$
HO_2			
R 3.12	$HO_2 + OH \longrightarrow H_2O + O_2$	300-2000	$4.81 \times 10^{-11} \exp^{2.08\,kJ/RT}$
R 3.13	$HO_2 + O \longrightarrow OH + O_2$	300-2500	$2.91 \times 10^{-11} \exp^{-1.66\,kJ/RT}$
R 3.14	$HO_2 + H \longrightarrow 2\,OH$	300-2500	$2.81 \times 10^{-10} \exp^{-3.66\,kJ/RT}$
R 3.15	$HO_2 + H \longrightarrow H_2 + O_2$	300-2500	$1.1 \times 10^{-10} \exp^{-109\,kJ/RT}$
R 3.16	$HO_2 + H_2 \longrightarrow H_2O_2 + H$	300-2500	3.01×10^{-12}
R 3.17	$HO_2 + H_2 \longrightarrow H_2O_2 + H$	300-2500	$5 \times 10^{-11} \exp^{-109\,kJ/RT}$
R 3.18	$HO_2 + M \longrightarrow O_2 + H + M$	200-2200	$2.41 \times 10^{-8} \tau^{-1.18} \exp^{-203.1\,kJ/RT}$
H			
R 3.19	$O + H + M \longrightarrow OH + M$	300-2500	$4.36 \times 10^{-32} \tau^{-1}$
R 3.20	$H + H + M \longrightarrow M + H_2$	300-2500	$6.04 \times 10^{-33} \tau^{-1}$
R 3.21	$O_2 + H \longrightarrow OH + O$	500-2000	$2.94 \times 10^{-10} \exp^{-69.68\,kJ/RT}$
R 3.22	$O_2 + H + M \longrightarrow HO_2 + M$	200-2200	$1.94 \times 10^{-32} \tau^{-1}$
H_2			
R 3.23	$OH + H_2 \longrightarrow H_2O + H$	200-2400	$2.97 \times 10^{-12} \tau^{1.21} \exp^{-19.71\,kJ/RT}$
R 3.24	$O + H_2 \longrightarrow OH + H$	300-2500	$3.44 \times 10^{-13} \tau^{-2.67} \exp^{-26.27\,kJ/RT}$
O			
R 3.25	$O + O + M \longrightarrow O_2 + M$	200-4000	$5.21 \times 10^{-35} \exp^{7.48\,kJ/RT}$
R 3.26	$O + H_2O \longrightarrow OH + OH$	300-2000	$6.68 \times 10^{-13} \tau^{2.6} \exp^{-63.52\,kJ/RT}$

The initial temperature is $T_0 = 20\,000\,\mathrm{K}$, which is equivalent to the voltage U of approximately 21 kV. The initial pressure is $p_0 = 1\,\mathrm{GPa}$ and the initial number of species is $n_{s,0} = n_{H_2O,0} = 3 \times 10^{22}$. During the pulse $t_{pulse} = 10\,\mathrm{ns}$ (sparse area) the temperature T and *n scale* stay almost constant. The number of species n_s changes only slightly during t_{pulse}. This is due to the chosen reactions in table 4.1 and 4.2. After t_{pulse}, T and *n scale* drop rapidly and the reactions lead to drastic changes of n_s in the expansion phase from 10 ns to 1 µs. The most of hydrogen peroxide is created within 10 ns to 100 ns.

At ignition, the number of water species n_{H_2O} drops from $n_{H_2O,0} = 3 \times 10^{22}$ to 4.75×10^{20} and starts to recover after t_{pulse} to 2.90×10^{22}. The number of hydro-

gen peroxide species $n_{H_2O_2}$ increases from 4.89×10^{18} to 3.24×10^{20}. Only these two numbers of species are rising significantly. The remaining numbers of species decrease after t_{pulse} as most of them are radicals and hence highly reactive. As Medodovic and Locke derived, reaction R 3.6 in table 4.2 is the main reaction for the hydrogen peroxide production. The rate constant shows almost no hydrogen peroxide production if the temperature is too high.

In view of this heat sensibility of the H_2O_2 production, the model shows this aspect, which can be seen during t_{pulse} because H_2O_2 has the lowest density due to the high temperature. If the reaction rate of reaction R 3.6 is set to 0, the H_2O_2 density after t_m is approximately $1.8 \times 10^{14}\,cm^{-3}$, which can be considered as zero compared to the total amount of species. As this model is based on the model in [45], this indicates correct modeling in this thesis. At any given time, the mass ratio of H and O is 2 : 1. This ensures and confirms that the number of species remains unchanged and that the GKM is a closed system.

In total, $N_{total} = 1.77 \times 10^{19}$ water species are treated within the initial volume V_0 of radius $r_0 = 25\,\mu m$ for $t = 10\,min$ at $f = 15\,Hz$ related to the initial density $n_0 = 3 \times 10^{22}\,cm^{-3}$. The calculation of the total number of species of the model $N_{M'}$ is:

$$N_{M'} = n_s \cdot \frac{1}{cm^3} \cdot t \cdot f \cdot V(r_0). \tag{4.9}$$

The factor $\frac{1}{cm^3}$ results from the standard volume which is set for the model. With respect to $n_{H_2O_2}$ of 3.24×10^{20} calculated with the Global Kinetic Model, this yields $N_{H_2O_2'} = 1.91 \times 10^{17}$ species. The efficiency of the H_2O_2 production is 1.1 %.

Considering the H_2O_2 concentration for $T_0 = 20\,000\,K$ of $c_{20\,kK} \approx 32\,\mu mol\,L^{-1}$ (see fig. 4.7), the species measured in the discharge chamber volume of $V_{chamber} = 25\,mL$ is about $N_{H_2O_2} = 4.82 \times 10^{17}$ species. The calculation for the total number of species of the measurement N_m is:

$$N_m = c_T \cdot V_{chamber} \cdot N_A. \tag{4.10}$$

N_A is the Avogadro constant.

Comparing $N_{H_2O_2'}$ and $N_{H_2O_2}$, they are of the same magnitude. For the initial pressure of 1 GPa, an initial radius of 73 µm would fit the measured concentration $c_{20\,kK}$. If the initial pressure of the model is changed to 10 GPa, which refers to the initial temperature $T_0 = 20\,000\,K$ of the voltage $U \approx 21\,kV$ by the cavitation theory (see. fig 4.6), the number of hydrogen peroxide species $n_{H_2O_2}$ is 4.39×10^{20} and an initial radius of 30 µm would match the measured concentration $c_{20\,kK}$ better.

The overall evolution of the number of species is similar for different initial pressures due to the slightly stronger and earlier decline of the T and n *scale* (see. fig. A.1 in the appendix A). In general, n_s increases proportionally with higher initial pressure p_0. The number of species as a function of the time with different initial temperature can be seen in the appendix (see. see. fig. A.2 and A.3 in the appendix A). The evolution shape characteristics of the number of species increases with the initial temperature. This can be explained by the temperature depending reactions.

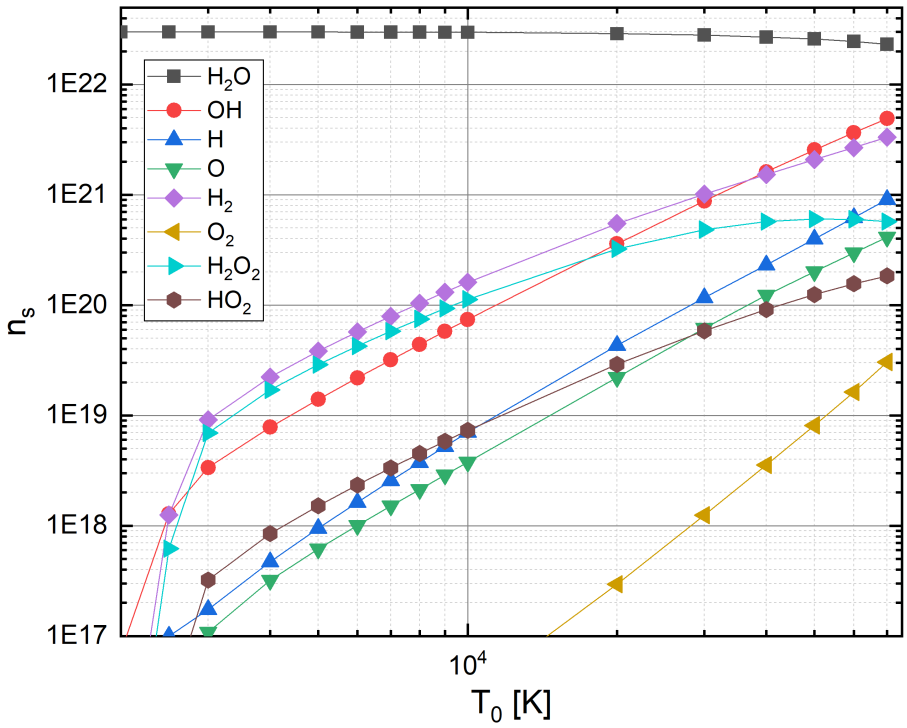

Figure 4.9: Number of species n_s as a function of the initial temperature T_0 after the modeling time $t_\mathrm{m} = 10\,\mu\mathrm{s}$. The initial pressure is $p_0 = 1\,\mathrm{GPa}$ and the initial number of species is $n_{\mathrm{s},0} = n_{\mathrm{H_2O},0} = 3 \times 10^{22}$.

The number of species n_s after the modeling time $t_\mathrm{m} = 10\,\mu\mathrm{s}$ as a function of the initial temperature T_0 is depicted in figure 4.9. The evolution of n_s rises quickly from 2500 K to 10 000 K. Only the molecular oxygen production starts after 10 000 K. From 10 000 K to 70 000 K, the increase of n_s is small. Within the initial temperature range of 2500 K to 20 000 K, the production of hydrogen peroxide can be considered. If T_0 is higher, the production of all other species is dominant, especially the production of hydroxide. Besides water, the number of molecular hydrogen species is the highest until 35 000 K. The number of molecular oxygen is the lowest for all T_0, which is correct in view of the hydrogen to oxygen ratio of 2 : 1. Produced hydroxide could form hydrogen peroxide when the bubble collapses and the species are mixed with the water bulk.

For comparison of the overall trend, the number of hydrogen peroxide species $N_{\mathrm{H_2O_2}}$, after $t_\mathrm{m} = 10\,\mu\mathrm{s}$ of the GKM according to equation (4.9) (line + symbols) and the measured number of hydrogen peroxide species $N_{\mathrm{H_2O_2}}$ according to equation (4.10) (symbols) as a function of the estimated initial temperature T_0 have been plotted in figure 4.10. The error calculation for the number of hydrogen peroxide species is $\Delta N_{\mathrm{H_2O_2}} = V_\mathrm{chamber} \cdot N_\mathrm{a} \cdot \Delta c_\mathrm{T}$.

It can be seen that the magnitudes are in the same order for $T_0 > 14\,000\,\mathrm{K}$. Referring to the model, $N_{\mathrm{H_2O_2}}$, reaches its maximum at $T = 50\,000\,\mathrm{K}$ and decays afterwards for higher T_0, which indicates the destruction of these species due to temperature sensitivity. This phenomena cannot be seen in the measurement. Either the voltage is not sufficient to reach the destruction or the model is not complete. A combination of all three speculations is most likely. One major weakness of the

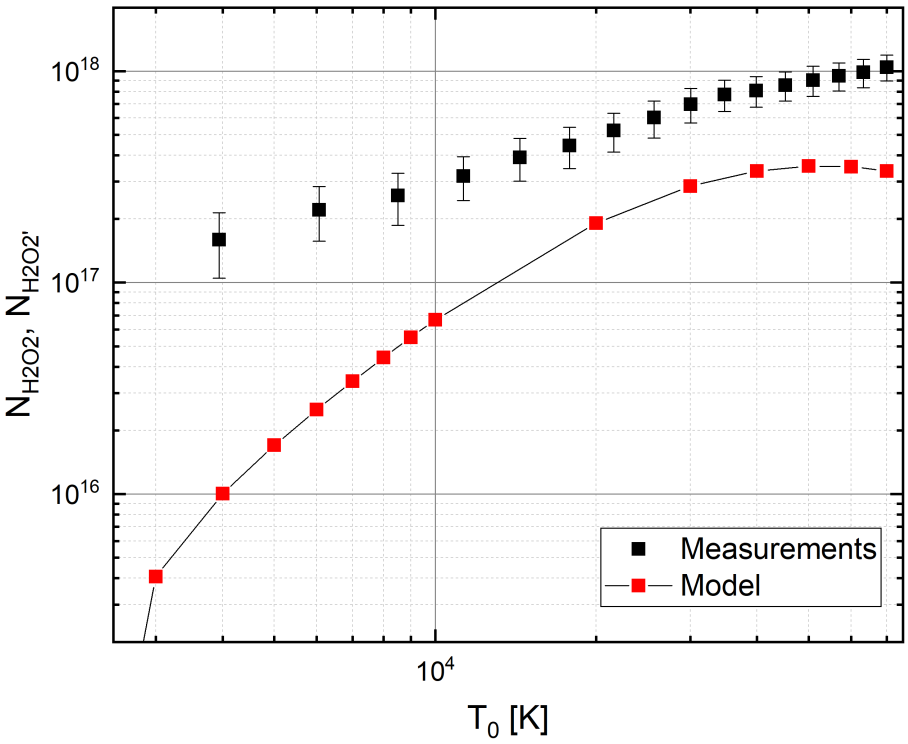

Figure 4.10: Number of hydrogen peroxide species $N_{H_2O_2'}$ after $t_m = 10\,\mu s$ of the GKM (line + symbols) and the measured number of hydrogen peroxide species $N_{H_2O_2}$ (symbols) as a function of the estimated initial temperature T_0. Both numbers are scaled to the volume of the chamber of 25 mL.

temperature estimation is the assumption of the ideal gas law (see eq. (4.5)). The ignition of the plasma occurs in fully ionized water of the density $n_0 = 3 \times 10^{22}\,cm^{-3}$. In this high density, a quantum approach of the plasma with the Fermi-Dirac distribution can be considered.

Generally, changing the initial pressure to the matching voltage and initial temperature according to the cavitation theory should result in better estimation of the density relating to the initial volume of 25 µm. Concerning the estimated initial temperature range from cavitation theory (see. fig. 4.7) in section 4.3, the primary reactions, which are valid below 2000 K in Medodovic's and Locke's model [45], would be valid for a longer time range than t_{pulse} because the temperature range is higher. Hence, the time frame of the primary reactions should be valid until the temperature of 2000 K is reached. This argues the assumption of validity of the primary reactions for the GKM for the complete modeling time t_m as 2000 K is reached shortly before t_m.

Measurements of other species than hydrogen peroxide is needed for more comparing point to improve the model. For example, results of observations of H and O with optical emission spectroscopy need to be included to this model. For any given initial temperature derived from the voltage, the right initial pressure according to the cavitation theory needs to be taken. In conclusion, the GKM shows good results for the hydrogen peroxide density prediction in comparison to the measurements. This indicates correct assumptions for the model and for the cavitation theory.

4.5 Quantum plasma

Based on the cavitation theory, the initial temperature T_0 range of the discharge is 3000 K to 70 000 K. T_0 is dependent on the discharge voltage and it is derived from the cavitation theory [12]. In this section, the initial temperature T_0 is denoted as the temperature T. With the 10 ns pulse and the rise time of 2 ns, the ignition is assumed to ionize the water fully at the density of $n_0 = 3 \times 10^{28}\,\mathrm{m}^{-3}$. The density of the electrons n_e is assumed to be equal to n_0 at the time of the ignition. This can be described as a quantum plasma as degeneracy occurs and the Pauli exclusion principle leads to repulsion of the electrons in the plasma which causes the majority of the pressure inside the bubble rather than the thermal energy at the ignition. A plasma is considered quantum if the Fermi energy E_f is higher than the thermal energy E_th:

$$E_\mathrm{f} > E_\mathrm{th} \tag{4.11}$$

with

$$E_\mathrm{f} = \frac{\hbar^2}{2m_\mathrm{e}}(3\pi^2 n_\mathrm{e})^{2/3} \tag{4.12}$$

and

$$E_\mathrm{th} = \frac{3}{2}\,k_\mathrm{b}T. \tag{4.13}$$

For simplicity reason, E_th in case of free electrons is taken. The electron mass is m_e, the reduced Plank constant is $\hbar$ and k_b is the Boltzmann constant. For $n_\mathrm{e} = 3 \times 10^{28}\,\mathrm{m}^{-3}$, the Fermi energy E_f is $5.64 \times 10^{-19}\,\mathrm{J}$. The thermal energy E_th for $T = 27\,000\,\mathrm{K}$ is $5.59 \times 10^{-19}\,\mathrm{J}$. According to the definition above, initial temperatures below $T = 27\,000\,\mathrm{K}$ are considered as a quantum plasma. Hence, the Fermi-Dirac statistic $f_\mathrm{FD}(E)$ is needed instead of the Maxwell-Boltzmann statistic,

$$f_\mathrm{FD}(E,T) = \frac{1}{\exp\frac{E-\mu}{k_\mathrm{b}T}+1}. \tag{4.14}$$

The probability to find a particle at a state of the energy E at the temperature T is $f_\mathrm{FD}(E,T)$. μ is the temperature dependent chemical potential. In case of $T = 0$ in a solid state, the chemical potential equals the Fermi energy E_f which is the maximal kinetic energy of an electron. This equals $f_\mathrm{FD}(E < \mu, 0) = 1$ and $f_\mathrm{FD}(E > \mu, 0) = 1$.

To evaluate the average energy distribution of the electrons, the density of state $D(E)$ in 3-dimensions is needed:

$$D(E) = \frac{(2m_\mathrm{e})^{3/2}}{2\pi^2\hbar^3}\sqrt{E}. \tag{4.15}$$

The total number of electrons $N(T)$ can be calculated with the following integration:

$$N(T) = \int_0^\infty D(E) \cdot f_\mathrm{FD}(E,T)\,dE. \tag{4.16}$$

As this integral represents the standardization and has to be equal to $N_\mathrm{e} = 3 \times 10^{28}$ for each temperature, the chemical potential μ has to be adapted. Exemplary, only

one ignition temperature will be considered in the following. In case of $T = 8000\,\mathrm{K}$, μ has to be approximately the Fermi energy of $E_\mathrm{f} \approx 5.64 \times 10^{-19}\,\mathrm{J}$ for the total number of electron to be N_e. The integration limit can be set from 0 to 100 eV for simplifying the calculation.

The average energy $\bar{E}'_\mathrm{FD}(T)$ is defined as:

$$\bar{E}'_\mathrm{FD}(T) = \frac{1}{N(T)} \int_0^\infty E \cdot D(E) \cdot f_\mathrm{FD}(E,T)\, dE, \tag{4.17}$$

and yields $\bar{E}'_\mathrm{FD}(T = 8000\,\mathrm{K}) \approx 2.6\,\mathrm{eV}$ for the given case.

The Maxwell-Boltzmann distribution, expressed in dependency of the energy $G_\mathrm{MB}(E,T)$, is:

$$G_\mathrm{MB}(E,T) = \frac{2}{k_\mathrm{b} T \sqrt{\pi}} \Big(\frac{E}{k_\mathrm{b} T}\Big)^{3/2} \exp^{-\frac{E}{k_\mathrm{b} T}}. \tag{4.18}$$

and the average energy $\bar{E}'_\mathrm{MB}(E,T)$ can be calculated with

$$\bar{E}'_\mathrm{MB}(T) = \int_0^\infty E \cdot G_\mathrm{MB}(E,T)\, dE. \tag{4.19}$$

This equals an average energy of $\bar{E}'_\mathrm{MB}(T = 8000\,\mathrm{K}) \approx 1\,\mathrm{eV}$. The Maxwell-Boltzmann distribution has to be calculated with the temperature $T = 20\,000\,\mathrm{K}$ to result an average energy of 2.6 eV

Detailed information to the distributions and derivations can be found in literature [58].

The number of electrons per unit energy $\frac{dN_\mathrm{FD}(E,T)}{dE}$ for the Fermi-Dirac distribution is given as

$$\frac{dN_\mathrm{FD}(E,T)}{dE} = D(E) \cdot f(E,T) \tag{4.20}$$

and the number of electrons per unit energy $\frac{dN_\mathrm{MB}(E,T)}{dE}$ for the Fermi-Dirac distribution is

$$\frac{dN_\mathrm{MB}(E,T)}{dE} = N_\mathrm{e} \cdot G(E,T). \tag{4.21}$$

In figure 4.11, the Fermi-Dirac distribution for $T = 8000\,\mathrm{K}$ (solid) and the Maxwell-Boltzmann distribution for $T = 8000\,\mathrm{K}$ (dashed) and $T = 20\,000\,\mathrm{K}$ (dashed doted) can be seen. For the same total amount of electrons, more electrons are distributed in higher energies in the Fermi-Dirac distribution due to the Pauli exclusion principle for $T = 8000\,\mathrm{K}$. The average energy for the Maxwell-Boltzmann distribution is 1 eV, but 2.6 eV for the Fermi-Dirac distribution. If the Maxwell-Boltzmann is calculated with $T = 20\,000\,\mathrm{K}$, the avarage energy is 2.6 eV.

In correlation to the estimated initial temperature based on the cavitation theory in section 4.3, the relation between the energy and the temperature are identical for a classical ideal gas and for a quantum ideal gas in non-relativistic case The caloric equation of state for the latter the quantum ideal gas is [59]

$$E = \frac{3}{2}\, pV. \tag{4.22}$$

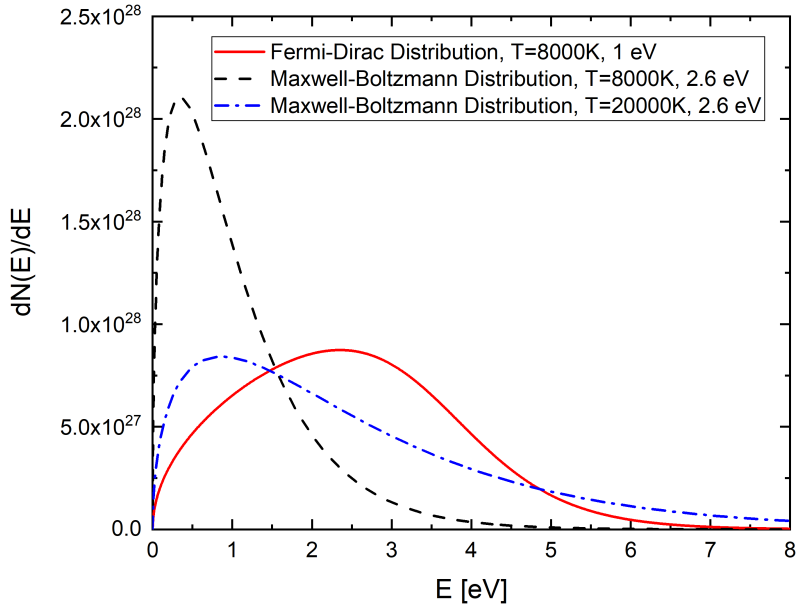

Figure 4.11: Number of electrons per unit energy $dN(E)/dE$ as a function of the energy E for Fermi-Dirac distribution for $T = 8000\,\mathrm{K}$ (solid) and the Maxwell-Boltzmann distribution for $T = 8000\,\mathrm{K}$ (dashed) and $T = 20\,000\,\mathrm{K}$ (dashed doted). The average energy can be seen in the legend. The total number of electrons are 3×10^{28}.

Consequently, the estimated temperatures in section 4.3, which considers the Maxwell-Boltzmann distribution and $E = {}^3\!/_2\, k_\mathrm{b} T$, are shifted by a factor of 2.6 when the Fermi-Dirac distribution is considered. With respect to the H_2O_2 concentration as a function of the derived initial temperature (see. fig 4.7), for example, the temperature of 20 000 K would be 8000 K. The initial temperatures in figure 4.10 must underlie the same shift. For this reason, the initial temperature for $U = 21\,\mathrm{kV}$ should be $T_0 = 8000\,\mathrm{K}$.

For the Global Kinetic Model, the consideration of a quantum plasma would not change the result, as the model only includes the rate constants. More information to each reaction in table 4.1 and 4.2 is needed e.g. the cross section and mean free time to calculate the rate constants considering the Fermi-Dirac distribution. Nevertheless, the results of the model should be correct as the average energy is important for the reactions. With consideration of the shift of the factor 2.6 of the Fermi-Dirac distribution and the Maxwell-Boltzmann distribution (see. fig 4.11, the calculation with the Maxwell-Boltzmann distribution can be taken for the Fermi-Dirac distribution. Accordingly, the initial temperature for the calculated number of species as a function of the time in fig 4.8 is $T_0 = 8000\,\mathrm{K}$ instead of $T_0 = 20\,000\,\mathrm{K}$.

Based on this considerations, the Fermi-Dirac statistic should give more realistic estimation of the energy distribution at the ignition point. Further work should take this aspect into account.

5 Conclusion and Outlook

The influences of the parameters treatment time, discharge frequency and discharge voltages on the hydrogen peroxide production in nanosecond pulse discharges in distilled water have been investigated. Based on the cavitation theory [12], the initial temperature has been estimated to examine the dependency of the hydrogen peroxide production to the initial temperature. In addition, a first modeling of the species production during the pulse via the Global Kinetic Model has been performed. Furthermore, the consideration of the Fermi-Dirac statistic for quantum plasma has been analyzed according to the assumed initial plasma density and temperature.

At first, it is important to mention that the calibration of the hydrogen peroxide test kit turned out to be difficult. Technical and instrumental errors could contribute to the shift of the calibration or more likely, the oxidation of the test kit could change the molar extinction coefficient due to density changes. Hence, calibration should be performed once if the kit is new and once before the kit is empty. By comparing both calibrations, a more precise statement about the possible causes of the calibration shift could be established. Nevertheless, tracking the measurements and the used test kit is indispensable for precise concentration calculation.

For the given experimental setup, the hydrogen peroxide concentration is in magnitude of $\mu\mathrm{mol\,L^{-1}}$. For the reference case at a discharge voltage of 20 kV, discharge frequency of 15 Hz and treatment time of 10 min, the hydrogen peroxide concentration is $(30 \pm 7)\,\mu\mathrm{mol\,L^{-1}}$. The hydrogen peroxide production increases linear with the treatment time and the discharge frequency. This finding could not be valid if the chosen treatment time is too long and if the frequency is too high. According to the initial volume of $r_0 = 25\,\mu\mathrm{m}$ treated by the plasma and the volume of the chamber of 25 mL, it is unlikely that hydrogen peroxide production saturates, especially with a maximal treatment time of 20 min. On the other hand, the discharge frequency would affect the discharge process, if the frequency is high enough to ignite a new discharge within the afterglow of the previous one. Hence, the hydrogen peroxide production will not be linear if the frequency is higher than the duration of the discharge process. For a frequency range of 1 Hz to 100 Hz, the described case does not occur.

In contrast, with increasing discharge voltage, the hydrogen peroxide production increases fast and then saturates in a sigmoidal form. This is due to temperature dependency of chemical reactions. Higher voltages result in higher initial pressure and temperature. The temperature of the discharge voltage is estimated by cavitation theory [12]. As the dependency of the initial pressure and the discharge voltage is $p_0 \propto U^2$, further increase of the voltage will not rise the temperature linearly. The optimal voltage for the maximal hydrogen peroxide production rate is at $U = 21\,\mathrm{kV}$ with the given experimental setup.

During the measurement, the electrode distance has shown an impact on the electrical field at the tip and consequently on the hydrogen peroxide production. Due to sign of wear, an electrode of another material could be considered for more stable and reproducible hydrogen peroxide production. The influence of the electrode gap distance should be investigated.

Measurements of the discharge power have to be performed, to examine the effectiveness of the hydrogen peroxide production of this nanosecond pulse discharge,. Additionally, a theoretical model of pulsed discharges in water by Lu et al. [11] could lead to a deeper understanding of the distribution of the discharge power and the overall discharge process if the model is modified to fit the given plasma in this thesis.

Moreover, a Global Kinetic Model based on Medodovic and Lockes model [45] for prediction of the species evolution during the discharge was used. The examined species are H_2O_2, OH, H, O, H_2, O_2, H_2O_2 and HO_2. The results obtained from the model for the number of hydrogen peroxide species at the initial temperature $T_0 = 20\,000\,\mathrm{K}$, which correlate to a voltage of approximately $U \approx 21\,\mathrm{kV}$, are in good agreement with the experimental measurements. This is a good starting point for further investigation of the species production in a nanosecond pulsed discharge. A separation of the validity of the primary and secondary chemical reactions during the discharge process could improve the model.

Nevertheless, more measurements of other species than hydrogen peroxide are needed to improve the model. Observations of H and O by optical emission spectroscopy need to be included in this modeling. Furthermore, concentration of OH by direct absorption or chemical dosimetry could be investigated. For higher and more effective hydrogen peroxide production, gaseous oxygen or active carbon bubbling could be introduced to the discharge chamber as other research groups have shown [41, 44].

Finally, in respect to the assumed plasma density of fully ionized water of the density $3 \times 10^{28}\,\mathrm{m}^{-3}$, the Fermi-Dirac distribution rather than the Maxwell-Boltzmann distribution needs to be considered for the initial temperature estimation depending on the discharge voltage. The initial temperature for $U = 21\,\mathrm{kV}$ would be $8000\,\mathrm{K}$ instead of $20\,000\,\mathrm{K}$. However, considering the Fermi-Dirac distribution for the initial temperature of the Global Kinetic Model yields wrong prediction of species density as the rate constant of the chemical reactions are of Maxwell-Boltzmann distribution. A solution needs to be found for this dilemma for more realistic modeling.

Bibliography

[1] M. Sato, T. Ohgiyama, and J. Clements, "Formation of chemical species and their effects on microorganisms using a pulsed high-voltage discharge in water", *IEEE Transactions on Industry Applications*, vol. 32, no. 1, pp. 106–112, Feb. 1996, ISSN: 00939994. DOI: 10.1109/28.485820.

[2] M. Sahni, W. C. Finney, and B. R. Locke, "Degradation of aqueous phase polychlorinated biphenyls (pcb) using pulsed corona discharges", *Journal of Advanced Oxidation Technologies*, vol. 8, no. 1, Jan. 2005, ISSN: 2371-1175, 1203-8407. DOI: 10.1515/jaots-2005-0117.

[3] S. Mededovic and B. R. Locke, "Side-chain degradation of atrazine by pulsed electrical discharge in water", *Industrial & Engineering Chemistry Research*, vol. 46, no. 9, pp. 2702–2709, Apr. 2007, ISSN: 0888-5885, 1520-5045. DOI: 10.1021/ie070020a.

[4] P. Šunka, "Pulse electrical discharges in water and their applications", *Physics of Plasmas*, vol. 8, no. 5, pp. 2587–2594, May 2001, ISSN: 1070-664X, 1089-7674. DOI: 10.1063/1.1356742.

[5] D. Mariotti, J. Patel, V. Švrček, *et al.*, "Plasma-liquid interactions at atmospheric pressure for nanomaterials synthesis and surface engineering", *Plasma Processes and Polymers*, vol. 9, no. 11–12, pp. 1074–1085, Dec. 2012, ISSN: 16128850. DOI: 10.1002/ppap.201200007.

[6] W. G. Graham and K. R. Stalder, "Plasmas in liquids and some of their applications in nanoscience", *Journal of Physics D: Applied Physics*, vol. 44, no. 17, p. 174 037, May 2011, ISSN: 0022-3727, 1361-6463. DOI: 10.1088/0022-3727/44/17/174037.

[7] I. Adamovich, S. D. Baalrud, A. Bogaerts, *et al.*, "The 2017 plasma roadmap: Low temperature plasma science and technology", *Journal of Physics D: Applied Physics*, vol. 50, no. 32, p. 323 001, Aug. 2017, ISSN: 0022-3727, 1361-6463. DOI: 10.1088/1361-6463/aa76f5.

[8] J. E. Foster, "Plasma-based water purification: Challenges and prospects for the future", *Physics of Plasmas*, vol. 24, no. 5, p. 055 501, May 2017, ISSN: 1070-664X, 1089-7674. DOI: 10.1063/1.4977921.

[9] R. J. Gilliom, "Pesticides in u.s. streams and groundwater", *Environmental Science & Technology*, vol. 41, no. 10, pp. 3408–3414, May 2007, ISSN: 0013-936X, 1520-5851. DOI: 10.1021/es072531u.

[10] P. C. Vandevivere, R. Bianchi, and W. Verstraete, "Review: Treatment and reuse of wastewater from the textile wet-processing industry: Review of emerging technologies", *Journal of Chemical Technology & Biotechnology*, vol. 72, no. 4, pp. 289–302, 1998. DOI: 10.1002/(SICI)1097-4660(199808)72:4<289::AID-JCTB905>3.0.CO;2-\#.

[11] X. Lu, Y. Pan, K. Liu, *et al.*, "Spark model of pulsed discharge in water", *Journal of Applied Physics*, vol. 91, no. 1, p. 24, 2002, ISSN: 00218979. DOI: 10.1063/1.1420765.

[12] K. Grosse, J. Held, M. Kai, *et al.*, "Nanosecond plasmas in water: Ignition, cavitation and plasma parameters", 2019.

[13] P. J. Bruggeman, M. J. Kushner, B. R. Locke, *et al.*, "Plasma–liquid interactions: A review and roadmap", *Plasma Sources Science and Technology*, vol. 25, no. 5, p. 053 002, Sep. 2016. DOI: 10.1088/0963-0252/25/5/053002.

[14] P. Bruggeman and C. Leys, "Non-thermal plasmas in and in contact with liquids", *Journal of Physics D: Applied Physics*, vol. 42, no. 5, p. 053 001, Mar. 2009, ISSN: 0022-3727, 1361-6463. DOI: 10.1088/0022-3727/42/5/053001.

[15] B. R. Locke and S. M. Thagard, "Analysis and review of chemical reactions and transport processes in pulsed electrical discharge plasma formed directly in liquid water", *Plasma Chemistry and Plasma Processing*, vol. 32, no. 5, pp. 875–917, Oct. 2012, ISSN: 0272-4324, 1572-8986. DOI: 10.1007/s11090-012-9403-y.

[16] B. R. Locke and K.-Y. Shih, "Review of the methods to form hydrogen peroxide in electrical discharge plasma with liquid water", *Plasma Sources Science and Technology*, vol. 20, no. 3, p. 034 006, Jun. 2011, ISSN: 0963-0252, 1361-6595. DOI: 10.1088/0963-0252/20/3/034006.

[17] Y. Seepersad, M. Pekker, M. N. Shneider, *et al.*, "On the electrostrictive mechanism of nanosecond-pulsed breakdown in liquid phase", *Journal of Physics D: Applied Physics*, vol. 46, no. 16, p. 162 001, Apr. 2013, ISSN: 0022-3727, 1361-6463. DOI: 10.1088/0022-3727/46/16/162001.

[18] A. Fridman, *Plasma Chemistry*. Cambridge University Press, 2008, ISBN: 978-0-511-54607-5. DOI: 10.1017/CBO9780511546075.

[19] H. Raether, "Electron avalanches and breakdown in gases", 1964.

[20] J. M. Meek and J. D. Craggs, "Electrical breakdown of gases", 1978.

[21] A. I. Gerasimov, "Water as an insulator in pulsed facilities (review)", *Instruments and Experimental Techniques*, vol. 48, no. 2, pp. 141–167, Mar. 2005, ISSN: 0020-4412, 1608-3180. DOI: 10.1007/s10786-005-0029-7.

[22] K. Schoenbach, J. Kolb, S. Xiao, *et al.*, "Electrical breakdown of water in microgaps", *Plasma Sources Science and Technology*, vol. 17, no. 2, p. 024 010, May 2008, ISSN: 0963-0252, 1361-6595. DOI: 10.1088/0963-0252/17/2/024010.

[23] J. Martin, "Nanosecond pulse techniques", *Proceedings of the IEEE*, vol. 80, no. 6, pp. 934–945, Jun. 1992, ISSN: 00189219. DOI: 10.1109/5.149456.

[24] R. Laenen, T. Roth, and A. Laubereau, "Novel precursors of solvated electrons in water: Evidence for a charge transfer process", *Physical Review Letters*, vol. 85, no. 1, pp. 50–53, Jul. 2000, ISSN: 0031-9007, 1079-7114. DOI: 10.1103/PhysRevLett.85.50.

[25] S. M. Korobeinikov, A. V. Melekhov, and A. S. Besov, "Breakdown initiation in water with the aid of bubbles", *High Temperature*, vol. 40, no. 5, pp. 652–659, Sep. 2002, ISSN: 1608-3156. DOI: 10.1023/A:1020420216579.

[26] F. Leipold, G. Yu, R. Stark, *et al.*, "Studies on the temporal development of electrical breakdown in water", in *Conference Record of the 2000 Twenty-fourth International Power Modulator Symposium*, IEEE, 2000, pp. 51–54, ISBN: 978-0-7803-5826-3. DOI: 10.1109/MODSYM.2000.896162.

[27] G. Touya, T. Reess, L. Pécastaing, *et al.*, "Development of subsonic electrical discharges in water and measurements of the associated pressure waves", *Journal of Physics D: Applied Physics*, vol. 39, no. 24, pp. 5236–5244, Dec. 2006, ISSN: 0022-3727, 1361-6463. DOI: 10.1088/0022-3727/39/24/021.

[28] P. Watson, W. Chadband, and M. Sadeghzadeh-Araghi, "The role of electrostatic and hydrodynamic forces in the negative-point breakdown of liquid dielectrics", *IEEE Transactions on Electrical Insulation*, vol. 26, no. 4, pp. 543–559, Aug. 1991, ISSN: 00189367. DOI: 10.1109/14.83669.

[29] N. Kuskova, "Distribution mechanism of leaders in water", *Zhurnal Tekhnicheskoi Fiziki*, vol. 53, no. 5, pp. 924–925, 1983.

[30] D. V. Tereshonok, N. Y. Babaeva, G. V. Naidis, *et al.*, "Pre-breakdown phenomena and discharges in a gas-liquid system", *Plasma Sources Science and Technology*, vol. 27, no. 4, p. 045 005, Apr. 2018, ISSN: 1361-6595. DOI: 10.1088/1361-6595/aab6d4.

[31] I. Marinov, O. Guaitella, A. Rousseau, *et al.*, "Cavitation in the vicinity of the high-voltage electrode as a key step of nanosecond breakdown in liquids", *Plasma Sources Science and Technology*, vol. 22, no. 4, p. 042 001, Jun. 2013, ISSN: 0963-0252, 1361-6595. DOI: 10.1088/0963-0252/22/4/042001.

[32] L. Rayleigh, "Viii. on the pressure developed in a liquid during the collapse of a spherical cavity", *The London, Edinburgh, and Dublin Philosophical Magazine and Journal of Science*, vol. 34, no. 200, pp. 94–98, Aug. 1917, ISSN: 1941-5982, 1941-5990. DOI: 10.1080/14786440808635681.

[33] F. R. Gilmore, "The growth or collapse of a spherical bubble in a viscous compressible liquid", 1952.

[34] M. S. Plesset and A. Prosperetti, "Bubble dynamics and cavitation", *Annual review of fluid mechanics*, vol. 9, no. 1, pp. 145–185, 1977.

[35] J. B. Keller and M. Miksis, "Bubble oscillations of large amplitude", *The Journal of the Acoustical Society of America*, vol. 68, no. 2, pp. 628–633, Aug. 1980, ISSN: 0001-4966. DOI: 10.1121/1.384720.

[36] D. V. Tereshonok, "Cavitation in liquid dielectric under nanosecond high-voltage impulse", *Journal of Physics D: Applied Physics*, vol. 50, no. 1, p. 015 603, Jan. 2017, ISSN: 0022-3727, 1361-6463. DOI: 10.1088/1361-6463/50/1/015603.

[37] A. Starikovskiy, Y. Yang, Y. I. Cho, *et al.*, "Non-equilibrium plasma in liquid water: Dynamics of generation and quenching", *Plasma Sources Science and Technology*, vol. 20, no. 2, p. 024 003, Apr. 2011, ISSN: 0963-0252, 1361-6595. DOI: 10.1088/0963-0252/20/2/024003.

[38] B. Halliwell and J. M. C. Gutteridge, *Free radicals in biology and medicine*, Fifth edition. Oxford University Press, 2015, ISBN: 978-0-19-871747-8.

[39] B. R. Locke, M. Sato, P. Sunka, *et al.*, "Electrohydraulic discharge and non-thermal plasma for water treatment", *Industrial & Engineering Chemistry Research*, vol. 45, no. 3, pp. 882–905, Feb. 2006, ISSN: 0888-5885, 1520-5045. DOI: 10.1021/ie050981u.

[40] A. Joshi, B. Locke, P. Arce, *et al.*, "Formation of hydroxyl radicals, hydrogen peroxide and aqueous electrons by pulsed streamer corona discharge in aqueous solution", *Journal of Hazardous Materials*, vol. 41, no. 1, pp. 3–30, Apr. 1995, ISSN: 03043894. DOI: 10.1016/0304-3894(94)00099-3.

[41] M. J. Kirkpatrick and B. R. Locke, "Hydrogen, oxygen, and hydrogen peroxide formation in aqueous phase pulsed corona electrical discharge", *Industrial & Engineering Chemistry Research*, vol. 44, no. 12, pp. 4243–4248, Jun. 2005, ISSN: 0888-5885, 1520-5045. DOI: 10.1021/ie048807d.

[42] P. Lukeš, *Water treatment by pulsed streamer corona discharge: Ph. D. thesis*. Institute of Plasma Physics, AS CR, 2001, ISBN: 978-80-902724-6-0.

[43] H. Wang, J. Li, X. Quan, *et al.*, "Formation of hydrogen peroxide and degradation of phenol in synergistic system of pulsed corona discharge combined with tio2 photocatalysis", *Journal of Hazardous Materials*, vol. 141, no. 1, pp. 336–343, Mar. 2007, ISSN: 03043894. DOI: 10.1016/j.jhazmat.2006.07.019.

[44] H. Wang, H. Guo, Q. Wu, *et al.*, "Effect of activated carbon addition on h2o2 formation and dye decoloration in a pulsed discharge plasma system", *Vacuum*, vol. 128, pp. 99–105, Jun. 2016, ISSN: 0042207X. DOI: 10.1016/j.vacuum.2016.03.015.

[45] S. Medodovic and B. R. Locke, "Primary chemical reactions in pulsed electrical discharge channels in water", *Journal of Physics D: Applied Physics*, vol. 42, no. 4, pp. 049 801–049 801, Feb. 2009, ISSN: 0022-3727, 1361-6463. DOI: 10.1088/0022-3727/42/4/049801.

[46] M. Sahni and B. R. Locke, "Quantification of hydroxyl radicals produced in aqueous phase pulsed electrical discharge reactors", *Industrial & Engineering Chemistry Research*, vol. 45, no. 17, pp. 5819–5825, Aug. 2006, ISSN: 0888-5885, 1520-5045. DOI: 10.1021/ie0601504.

[47] D. R. Grymonpré, W. C. Finney, and B. R. Locke, "Aqueous-phase pulsed streamer corona reactor using suspended activated carbon particles for phenol oxidation: Model-data comparison", *Chemical Engineering Science*, vol. 54, no. 15–16, pp. 3095–3105, Jul. 1999, ISSN: 00092509. DOI: 10.1016/S0009-2509(98)00428-X.

[48] H. C. Urey, L. H. Dawsey, and F. O. Rice, "The absorption spectrum and decomposition of hydrogen peroxide by light", *Journal of the American Chemical Society*, vol. 51, no. 5, pp. 1371–1383, May 1929, ISSN: 0002-7863, 1520-5126. DOI: 10.1021/ja01380a011.

[49] D. P. Nelson and L. A. Kiesow, "Enthalpy of decomposition of hydrogen peroxide by catalase at 25° c (with molar extinction coefficients of h2o2 solutions in the uv)", *Analytical Biochemistry*, vol. 49, no. 2, pp. 474–478, Oct. 1972, ISSN: 00032697. DOI: 10.1016/0003-2697(72)90451-4.

[50] R. Burlica, K.-Y. Shih, and B. R. Locke, "Formation of h 2 and h 2 o 2 in a water-spray gliding arc nonthermal plasma reactor", *Industrial & Engineering Chemistry Research*, vol. 49, no. 14, pp. 6342–6349, Jul. 2010, ISSN: 0888-5885, 1520-5045. DOI: 10.1021/ie100038g.

[51] G. Eisenberg, "Colorimetric determination of hydrogen peroxide", *Industrial & Engineering Chemistry Analytical Edition*, vol. 15, no. 5, pp. 327–328, 1943.

[52] E. Tütem, R. Apak, and F. Baykut, "Spectrophotometric determination of trace amounts of copper(i) and reducing agents with neocuproine in the presence of copper(ii)", *The Analyst*, vol. 116, no. 1, pp. 89–94, 1991, ISSN: 0003-2654, 1364-5528. DOI: 10.1039/AN9911600089.

[53] L. Pecci, G. Montefoschi, and D. Cavallini, "Some new details of the copper-hydrogen peroxide interaction", *Biochemical and Biophysical Research Communications*, vol. 235, no. 1, pp. 264–267, Jun. 1997, ISSN: 0006291X. DOI: 10.1006/bbrc.1997.6756.

[54] W. An, K. Baumung, and H. Bluhm, "Underwater streamer propagation analyzed from detailed measurements of pressure release", *Journal of Applied Physics*, vol. 101, no. 5, p. 053 302, Mar. 2007, ISSN: 0021-8979, 1089-7550. DOI: 10.1063/1.2437675.

[55] N. A. Lange, *Lange's handbook of chemistry*, 15. ed, ser. McGraw-Hill handbooks. McGraw-Hill, 1999, ISBN: 978-0-07-016384-3.

[56] W. Giedt, *Thermophysics*. Van Nostrand Reinhold Co., 1971.

[57] *Nist chemical kinetics database*, Accessed: 16-06-2019. [Online]. Available: https://kinetics.nist.gov/kinetics/index.jsp.

[58] K. Kopitzki and P. Herzog, *Einführung in die Festkörperphysik*, 6., überarb. Aufl., unveränd. Nachdr, ser. Studium. Vieweg + Teubner, 2009, ISBN: 978-3-8351-0144-9.

[59] T. Fließbach, "Ideales quantengas", in *Statistische Physik*. Spektrum Akademischer Verlag, 2010, pp. 247–258, ISBN: 978-3-8274-2527-0. DOI: 10.1007/978-3-8274-2528-7_30.

6 Acknowledgement

Zum Abschluss dieser Arbeit möchte ich mich bei allen Personen bedanken, die mich während der Anfertigung dieser Bachelorarbeit unterstützt und motiviert haben. Mein Dankeschön geht vor allem an:

- Prof. Dr. Achim von Keudell für die Beantwortung aufkommender Fragen, die Bereitstellung des Modell und die Möglichkeit meine Arbeit an dem Lehrstuhl für Experimentalphysik II durchzuführen zu dürfen.
- Dr. Laura Chauvet für die herzliche Unterstützung und Betreuung und für die große Hilfsbereitschaft.
- Jan Löwer für die unvergessliche Zeit im Büro, aufmunternde Gespräche, fleißiges Korrekturlesen und seine Hilfe.
- Die anderen Studierenden für die Unterstützung und schönen Unterhaltungen, insbesondere Steffen Schüttler.
- Alle Mitarbeiter und Techniker des Lehrstuhls für die Hilfsbereitschaft und Ratschläge, ganz besonders Katharina Grosse.

Abschließend möchte ich mich aufrichtig bei meiner Familie und Isabel Schreiber für die starke molarische Unterstützung bedanken.

A Appendix

A.1 Initial pressure variation

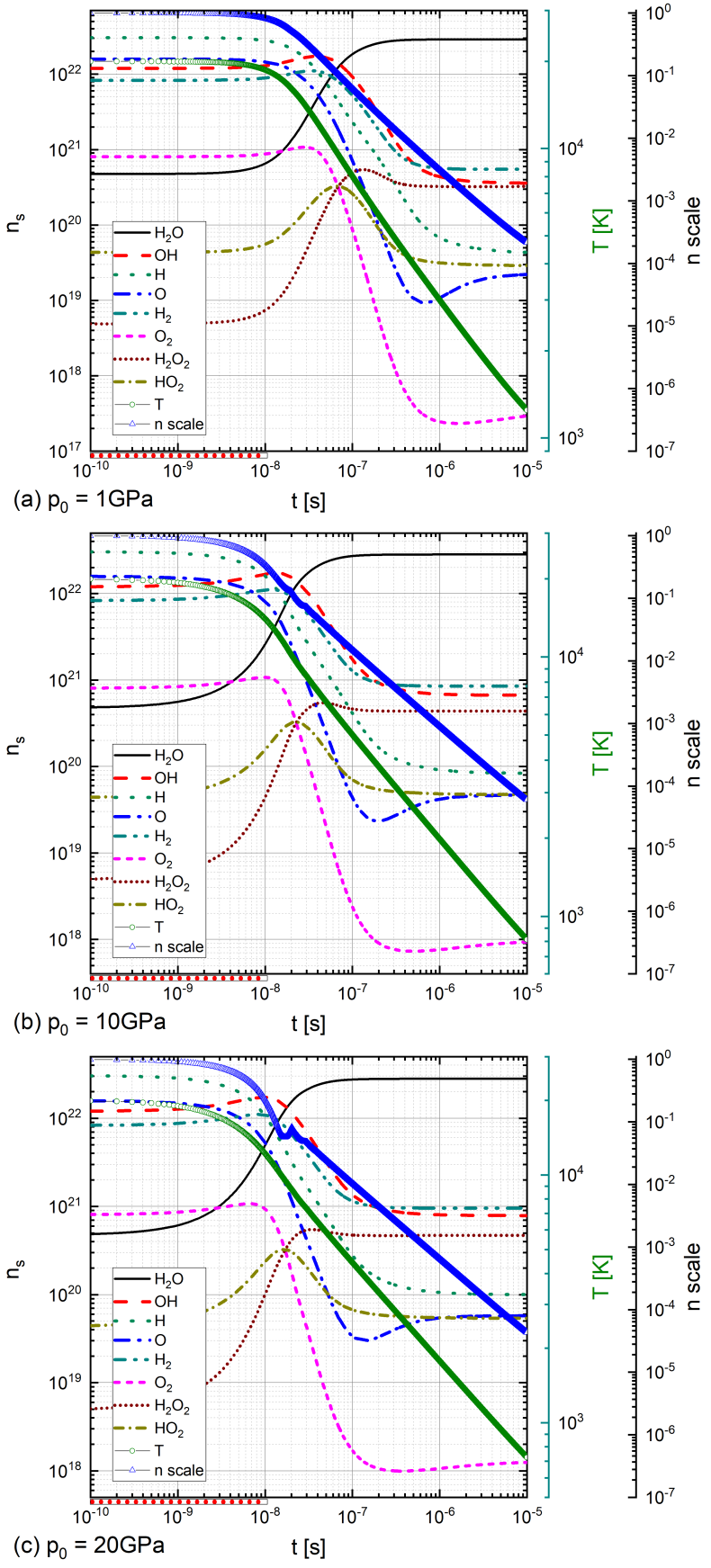

Figure A.1: Number of species n_s as a function of the initial temperature $T_0 = 20\,000\,\mathrm{K}$ after the modeling time $t_\mathrm{m} = 10\,\mu\mathrm{s}$. The initial pressures are (a) $p_0 = 1\,\mathrm{GPa}$; (b) $p_0 = 10\,\mathrm{GPa}$, (c) $p_0 = 20\,\mathrm{GPa}$ and the initial number of species is $n_{\mathrm{s},0} = n_{\mathrm{H_2O},0} = 3 \times 10^{22}$. The pulse duration is $t_\mathrm{pulse} = 10\,\mathrm{ns}$ (sparse area).

A.2 Initial temperature variation

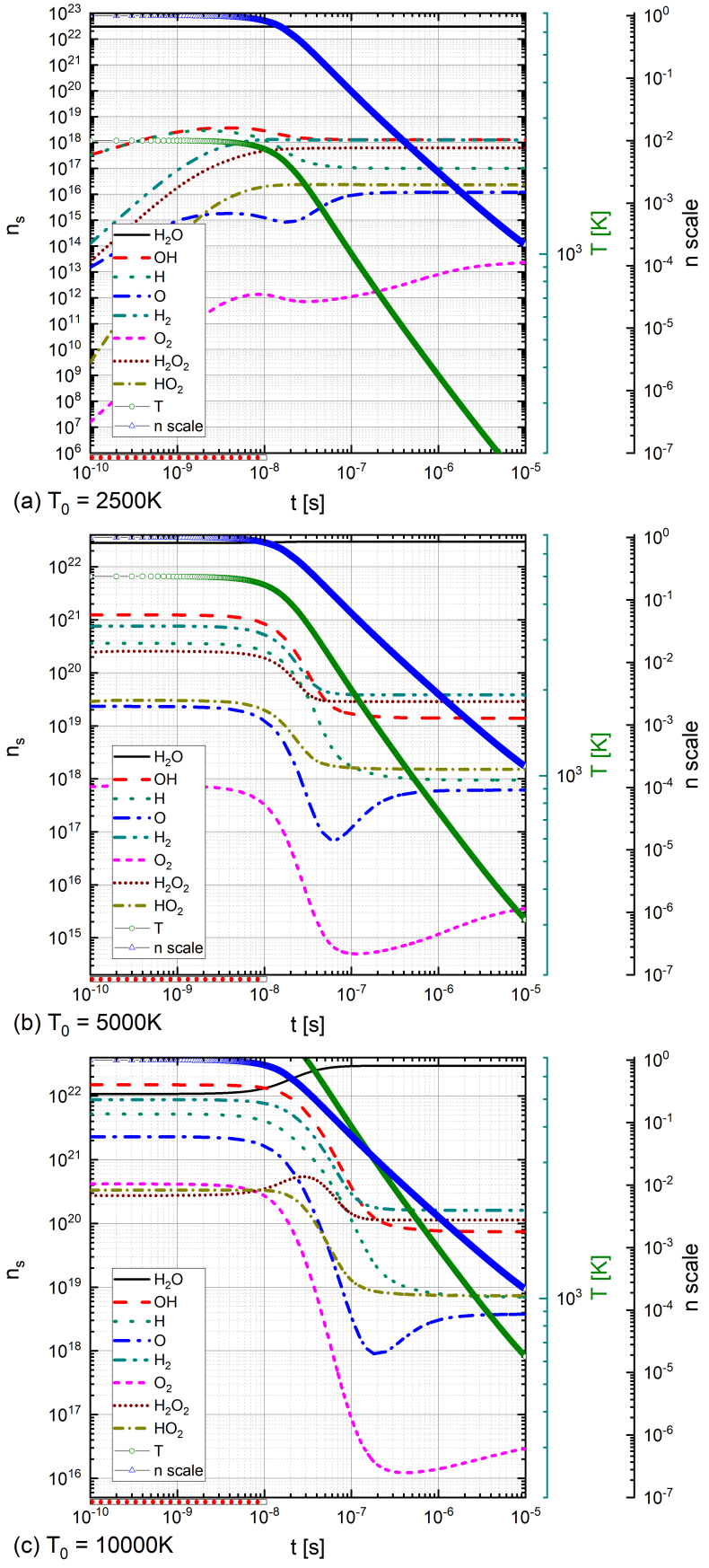

Figure A.2: Number of species n_s as a function of the initial temperatures (a) $T_0 = 2500\,\mathrm{K}$; (b) $T_0 = 5000\,\mathrm{K}$; (c) $T_0 = 10\,000\,\mathrm{K}$ after the modeling time $t_\mathrm{m} = 10\,\mu\mathrm{s}$. The initial pressure is $p_0 = 1\,\mathrm{GPa}$ and the initial number of species is $n_{\mathrm{s},0} = n_{\mathrm{H_2O},0} = 3 \times 10^{22}$. The pulse duration is $t_\mathrm{pulse} = 10\,\mathrm{ns}$ (sparse area).

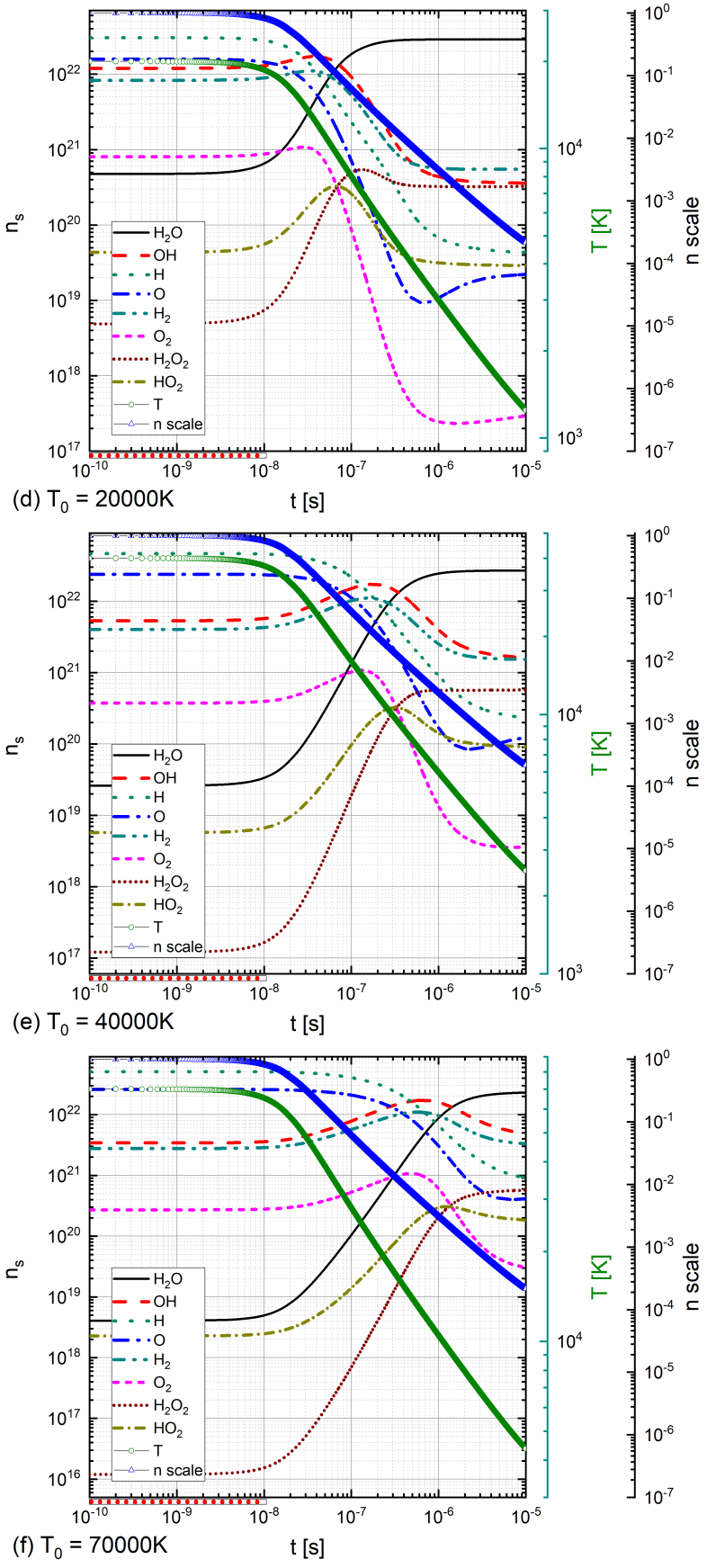

Figure A.3: Number of species n_s as a function of the initial temperatures (d) $T_0 = 20\,000\,\mathrm{K}$; (e) $T_0 = 40\,000\,\mathrm{K}$; (f) $T_0 = 70\,000\,\mathrm{K}$ after the modeling time $t_\mathrm{m} = 10\,\mu\mathrm{s}$. The initial pressure is $p_0 = 1\,\mathrm{GPa}$ and the initial number of species is $n_{\mathrm{s},0} = n_{\mathrm{H_2O},0} = 3 \times 10^{22}$. The pulse duration is $t_\mathrm{pulse} = 10\,\mathrm{ns}$ (sparse area).